



This is a repository copy of *Water–sediment flow modeling for field case studies in Southwest China*.

White Rose Research Online URL for this paper:
<http://eprints.whiterose.ac.uk/86324/>

Version: Accepted Version

Article:

Chen, R., Shao, S. and Liu, X. (2015) Water–sediment flow modeling for field case studies in Southwest China. *Natural Hazards*. ISSN 0921-030X

<https://doi.org/10.1007/s11069-015-1765-z>

Reuse

Unless indicated otherwise, fulltext items are protected by copyright with all rights reserved. The copyright exception in section 29 of the Copyright, Designs and Patents Act 1988 allows the making of a single copy solely for the purpose of non-commercial research or private study within the limits of fair dealing. The publisher or other rights-holder may allow further reproduction and re-use of this version - refer to the White Rose Research Online record for this item. Where records identify the publisher as the copyright holder, users can verify any specific terms of use on the publisher's website.

Takedown

If you consider content in White Rose Research Online to be in breach of UK law, please notify us by emailing eprints@whiterose.ac.uk including the URL of the record and the reason for the withdrawal request.



eprints@whiterose.ac.uk
<https://eprints.whiterose.ac.uk/>

Water-Sediment Flow Modeling for Field Case Studies in Southwest China

Ridong Chen¹, Songdong Shao² and Xingnian Liu^{3,*}

¹ State Key Laboratory of Hydraulics and Mountain River Engineering, College of Water Resource and Hydropower, Sichuan University, Chengdu 610065, China. Email: chenridong1984@163.com

² Department of Civil and Structural Engineering, University of Sheffield, Sheffield S1 3JD, UK (State Key Laboratory of Hydraulics and Mountain River Engineering, Sichuan University, Chengdu 610065, China). Email: s.shao@sheffield.ac.uk

^{3*} State Key Laboratory of Hydraulics and Mountain River Engineering, College of Water Resource and Hydropower, Sichuan University, Chengdu 610065, China. Email: scucrs@163.com (Author of Correspondence)

Abstract

The paper presents a highly robust numerical model to simulate water-sediment mixture flows in practical field studies. The model is composed of an integrated algorithm combining the finite element characteristic splitting method and finite volume Godunov scheme. The former maintains the generality and stability of the numerical algorithm while the latter ensures the conservation and accuracy of the model. The proposed model is first tested by three benchmark flow problems including flood flow in a pool, dam break over a mobile bed and morphological process of a dam removal. Then the model is applied to two practical field case studies to demonstrate its potential engineering values. The first case study is related to the damage of the Polo Hydropower Plant by a sediment flooding event. The second one is the investigation of a well-known 2013 dam break flooding that happened in the Tangjiashan Mountain. It is shown that the simulated water and sediment flows are in good agreement with the documented laboratory and field data and the numerical model is capable of providing useful information on the flow predictions thus making further engineering measures to mitigate these disasters.

Keywords: Water-sediment flow modeling; Southwest China; Flood; Sediment; Field study; Polo Hydropower Plant; Tangjiashan Mountain flood

1. Introduction

In China there are around 50,000 rivers with a coverage area being 100 km² and 1,500 rivers with a coverage area being 1000 km². Severe flood and sediment movement are typical features of these rivers due to soil erosion in the catchment area, which caused serious engineering concerns. Especially, the Southwest China region is characterized by mountainous topography and narrow valley, and thus quite a few large hydropower plants have been built to exploit the natural water resource. These dam constructions brought great benefit to the local economy, but meanwhile they also adversely influenced the balance between flow and sediment coexistences. In this sense, timely and accurate predictions of the flood and sediment flows could provide important information in the engineering field. However, the rivers in Southwest China most demonstrate large variation in the water levels and sediment transport capacities. In addition, the mobile bed is composed of different size of sediment materials, which made the process of bed evolution much more complex. Therefore, the development of an efficient and accurate numerical model for these mountainous rivers involves much more challenging tasks than those encountered in the plain rivers.

The accuracy of any water-sediment mixture flow models should rely on the underlying sediment mechanics. For example, Wang and Song (1995) summarized the sediment research status in Europe and America around the 20th century and Wang (1999) reviewed the river sedimentation issues in China. In recent years, great progresses have been made in the study of various sediment mechanics such as the transport capacity, bed form and resistance. For example, 1-D numerical models have been efficiently used for the simulation of flow and sediment processes across large spatial and temporal domains, including the CRS-1 model developed by Liu (2004) at Sichuan University and the HEC model developed by USACE (2003). In order to obtain more detailed flow information along the cross-sectional area, a variety of 2-D numerical models have been developed (Demirbilek and Nwogu, 2007), including the SMS model by Brigham University, RIVCOM by the Delft and MKE21 by the DHI. As these 2-D water-sediment flow models are very CPU efficient, and meanwhile can achieve sufficient accuracy in the flow simulations, they have been widely used in the engineering practice. In comparison, more complicated 3-D models are often used in some refined areas for the purpose of theoretical study and model verification (Liu et al., 2012). Most of the 2-D numerical models are based on the hydrodynamic equations together with different sediment transport modes, in which the 2-D Shallow Water Equations (SWEs) model could be the most widely adopted for large-scale river simulations. On the other hand, the commonly used numerical solution schemes are the Finite Difference method (FDM), Finite Element method (FEM) and Finite Volume method (FVM), respectively, to discretize the flow and sediment equations. Each numerical scheme has some kinds of advantage in certain flow problems but may not perform satisfactorily in a different situation. As a result, the combined or mixed solution schemes have been developed to deal with more complicated

41 issues, such as the FEM-based FVM, FVM-based FEM and hybrid FDM/FVM methods
42 (Guillou and Nguyen, 1999; Du, 2000; Casulli and Zanolli, 2002).

43

44 In order to investigate the practical sediment-laden flood flows in the field of Southwest
45 China, we should have a competent numerical model that is not only stable and efficient, but
46 also able to deal with complicated boundaries arising from the sediment transport and alluvial
47 deformation. The FEM-based characteristic splitting method and FVM-based Godunov
48 scheme have proved to be robust modeling techniques in numerous flow applications and
49 thus we will develop a hybrid numerical algorithm by combining the above two. The former
50 guarantees the generality and stability of the solution scheme while the latter ensures the
51 conservation and accuracy of the model. The hybrid model will be used to simulate two field
52 cases related to sediment flooding in the Southwest China and the computational findings
53 could provide useful information to mitigate the natural disasters in engineering practice.

54

55

56 **2. Water-Sediment Mixture Flow Model**

57

58 In the field of water-sediment mixture flow modeling, great achievements have been made in
59 the fundamental equations to describe the physical process and the numerical schemes to
60 solve these equations. Any robust numerical algorithm should possess not only the property
61 of compatibility, stability and convergence, but they should also demonstrate the feature of
62 conservation, non-dissipation/dispersion and computational efficiency/accuracy. In this
63 section, first we will introduce the governing equations in 2-D domain for the water-sediment
64 mixture flow and then the numerical solution technique using the FEM characteristic splitting
65 method and FVM Godunov scheme is developed. The hybrid numerical algorithm inherited
66 the advantages of both FEM and FVM and improved the numerical treatment of advection
67 term.

68

69 **2.1 Governing equations for water-sediment mixture flow**

70

71 The following 2-D shallow water equations (SWEs), sediment transport and bed deformation
72 equations are used for the water-sediment mixture flows as

$$73 \quad \frac{\partial \eta}{\partial t} + \nabla \cdot (h\mathbf{u}) = 0 \quad (1)$$

$$74 \quad \frac{d(h\mathbf{u})}{dt} = A_H h \nabla^2 \mathbf{u} - gh \nabla \eta - \frac{gn^2 |\mathbf{u}| \mathbf{u}}{h^{1/3}} \quad (2)$$

$$75 \quad \frac{d(hS)}{dt} = \alpha \omega (S^* - S) + A_H h \nabla^2 S \quad (3)$$

76
$$(1 - \xi) \frac{\partial z_b}{\partial t} + \nabla \cdot \mathbf{q}_b = \frac{\alpha \omega (S - S^*)}{\rho_s} \quad (4)$$

77 in which η = water surface; t = time; h = flow depth; $\mathbf{u} = (u, v)$ are the horizontal 2-D flow
 78 velocities; n = bed roughness; g = gravitational acceleration; S = sediment suspended load
 79 concentration; ω = sediment settling velocity; S^* = maximum suspended load carrying
 80 capacity; α = erosion-deposition coefficient (0.25 is used for deposition, 1.0 for erosion and
 81 0.5 for transition); z_b = movable bed layer thickness; ξ = bed porosity; ρ_s = density of
 82 sediment grain; and $\mathbf{q}_b = (q_{bx}, q_{by})$ are the horizontal 2-D sediment bed load transport in x
 83 and y directions.

84

85 Here it should be noted that the above water flow equations (1) - (2) are not influenced by
 86 any sediment transport parameters in equation (3) - (4), and thus they are represented in the
 87 uncoupled form, which is in contrast to those used by Cao et al. (2011). This is based on the
 88 rationale that the suspended load is not the dominant sediment transport mode in the present
 89 field case studies and the flow structure is not significantly modified by the existence of the
 90 sediment mixture.

91

92 The horizontal eddy viscosity coefficient A_H in equations (2) and (3) is represented as

93
$$A_H = C_s A \left[\left(\frac{\partial u}{\partial x} \right)^2 + 0.5 \left(\frac{\partial v}{\partial x} + \frac{\partial u}{\partial y} \right)^2 + \left(\frac{\partial v}{\partial y} \right)^2 \right]^{0.5} \quad (5)$$

94 in which C_s = Horcon coefficient, taken between 0.1 - 0.2 in this paper; and A = node
 95 influence area.

96

97 **2.2 Evaluations of relevant sediment parameters**

98

99 The choice of bed load transport equation is a difficult issue, as different formulations can
 100 predict the results within an error of several orders. Besides, the sediment bed load transport
 101 is also highly sensitive to the flow velocity, as the relationship between the two is not a linear
 102 function. Thus unrealistic bed deformations can be predicted if the formula is not correctly
 103 used. In this study, we will adopt the widely used Meyer-Peter formula as follows:

104
$$\mathbf{q}_b = 8 \sqrt{(s-1) g d_i^3} \frac{\mathbf{u}}{|\mathbf{u}|} \max(\tau_* - \tau_c, 0)^{1.5} \quad (6)$$

105 in which s = relative density of the sediment grain to water; d_i = sediment grain size of one

106 group; $\tau_* = \frac{n^2 |\mathbf{u}|^{1.5}}{(s-1) d_i h^{1/3}}$ is the flow shear stress; and $\tau_c = 0.047$ is the threshold shear stress

107 of grain initiation. As the Meyer-Peter formula covered a relatively wide range of sediment

108 grain sizes, it should be suitable for the field studies in Southwest China, in which most of the
109 river beds are covered by the highly graded sediment materials.

110

111 The threshold grain size separating the bed load and suspended load materials can be
112 determined by the so-called suspension index, which is represented by (Qian and Wan, 1983)

$$113 \quad R_z = \frac{\omega}{\kappa u_*} \quad (7)$$

114 in which $\kappa = 0.41$ is the von Karmon constant; and u_* = frictional velocity. From the case
115 studies on many field rivers in the Southwest China, the general guidelines stipulate that $R_z >$
116 4.166 falls into the bed load and $R_z < 4.166$ belongs to the suspended load (Liu, et al. 1991).

117

118 The sediment settling velocity is calculated by the following formula (Zhang, 1961)

$$119 \quad \omega = \sqrt{\left(13.95 \frac{\nu}{d}\right)^2 + 1.09 \frac{\gamma_s - \gamma}{\gamma} gd} - 13.95 \frac{\nu}{d} \quad (8)$$

120 where ν = kinematic viscosity of water; γ_s and γ = gravity density of sediment grain and
121 water, respectively.

122

123 The general form of sediment carrying capacity of the flow can be represented by

$$124 \quad S^* = k \left(\frac{U^3}{gh\omega} \right)^m \quad (9)$$

125 in which k and m = empirical sediment coefficient, whose values depend on the particular
126 river location. In practical sediment simulations, to address the non-uniformity of suspended
127 load transport and the bed materials adjustment arising from the alluvial deformation,
128 adequate modifications of equation (9) are provided by and Zhang (1998).

129

130

131 **3 Numerical Solution Schemes**

132

133 Here the proposed numerical solution method couples the FEM characteristic splitting with
134 FVM Godunov schemes to improve the computational efficiency and accuracy. To improve
135 the solution stability of advection-dominated flows, Zienkiewicz and Codina (1995)
136 developed the split characteristic based FEM scheme. This algorithm has the advantage of
137 simplicity and stability and is particularly suitable for the simulation of mountainous river
138 flows over relatively steep slope and complicated alluvial topographies. By following
139 Zienkiewicz and Codina (1995), the split schemes in both the spatial and temporal domains
140 are considered in this work.

141

142

143 On the other hand, the FVM based Godunov scheme is widely used to solve the SWEs type
 144 equations of nonlinear hyperbolic feature due to its well-balanced conservation property (Pu
 145 et al., 2012). Thus it can compensate for the drawback of FEM that cannot achieve the exact
 146 property conservation in all of the computational elements. Numerical schemes based on the
 147 Godunov are also quite efficient to treat the flows with large energy gradient as well as shock
 148 waves. By combining with the approximate Riemann solver, the computational efficiency is
 149 greatly improved when solving the momentum flux across the cells and higher order schemes
 150 can be easily implemented as a result.

151
 152 In the coupled FEM-FVM computations, the FVM Godnuov scheme is used to correct the
 153 deficiency cells except those on the boundaries after several time steps of FEM computation.
 154 So the conservation property of FEM scheme can be maintained by the coupled FVM scheme.
 155 Besides, the FEM uses a first-order accurate element, while the coupled model adopts the
 156 TVD algorithm which is second-order accurate. As the FEM and FVM methods use different
 157 storage systems to save the flow variables, frequent data interpolation and communication
 158 should be implemented to transfer the flow information between the two. A brief review of
 159 the coupled FEM-FVM solution procedure is provided below.

160
 161 The solution of water flow is first carried out based on the FEM scheme. Let $\mathbf{R} = \begin{bmatrix} hu \\ hv \end{bmatrix}$,

162 $\mathbf{r} = \begin{bmatrix} u \\ v \end{bmatrix}$, $\mathbf{q}_b = \begin{bmatrix} q_{bx} \\ q_{by} \end{bmatrix}$ and $\mathbf{i} = \begin{bmatrix} i_x \\ i_y \end{bmatrix}$, in which i_x and i_y are the slopes of the terrain, then the

163 solution procedure of matrix \mathbf{R}^{n+1} is

164 (1) First step: Solving the variation of velocity $\Delta\mathbf{R}^*$

$$165 \quad \Delta\mathbf{R}^* = \mathbf{R}^* - \mathbf{R}^n = -\mathbf{M}^{-1}\Delta t[(\mathbf{C}\mathbf{R} + \mathbf{K}_m\mathbf{r} - \mathbf{f}) - \Delta t(\mathbf{K}_s\mathbf{R} + \mathbf{f}_s)]^n \quad (10)$$

166 (2) Second step: Solving the variation of depth Δh

$$167 \quad \Delta h = \mathbf{M}^{-1}\Delta t[\mathbf{H}(\mathbf{R}^n + \theta_1\Delta\mathbf{R}^*) - \Delta t\theta_1\mathbf{G}\mathbf{p}^n - \mathbf{f}_h] \quad (11)$$

168 (3) Third step: Using Δh and correcting $\Delta\mathbf{R}^*$ to get the value at next time step t^{n+1}

$$169 \quad h^{n+1} = h^n + \Delta h \quad (12)$$

$$170 \quad \mathbf{R}^{n+1} = \mathbf{R}^n + \Delta\mathbf{R}^* - \mathbf{M}^{-1}\Delta t\mathbf{H}^T\mathbf{p}^n \quad (13)$$

171 The detailed definitions of relevant variables in equations (10) - (13) can be found in Chen et
 172 al. (2011) so they are not repeated here. The computational time step should satisfy the
 173 following Courant criterion

$$174 \quad \Delta t \leq C_{FL} \frac{l_{em}}{c + |\mathbf{u}|} \quad (14)$$

175 in which l_{em} = characteristic element size; $c = \sqrt{gh}$ is the gravity wave celerity in shallow
 176 water; and C_{FL} = Courant stability coefficient, taken as 0.3 ~ 0.7 in the present paper.

177 (4) Fourth step: Then the FVM Godunov scheme is applied to improve the FEM performance
 178 and the flow velocity field is updated by

$$179 \quad \mathbf{u}_i^p = \mathbf{u}_i^n - \frac{\Delta t}{\Delta} \sum_{j=1}^3 (\mathbf{F} \cdot \mathbf{n}_x + \mathbf{G} \cdot \mathbf{n}_y) \mathbf{l}_j \quad (15)$$

$$180 \quad \mathbf{u}_i^{n+1} = \mathbf{u}_i^p + \Delta t \mathbf{S}(\mathbf{u}_i^p) \quad (16)$$

181 in which p represents the prediction step; \mathbf{F} and \mathbf{G} = numerical flux in x and y directions,
 182 respectively; l = side length of the FV; and \mathbf{S} = source term. The numerical flux can be
 183 calculated by the general HLLC schemes as

$$184 \quad \mathbf{F}_{i+\frac{1}{2}}^{\text{hllc}} = \begin{cases} \mathbf{F}_L & 0 \leq S_L \\ \mathbf{F}_{*L} & S_L \leq 0 \leq S_*, \mathbf{F}_{*L} = \mathbf{F}_L + S_L(\mathbf{u}_{*L} - \mathbf{u}_L) \\ \mathbf{F}_{*R} & S_* \leq 0 \leq S_R, \mathbf{F}_{*R} = \mathbf{F}_R + S_R(\mathbf{u}_{*R} - \mathbf{u}_R) \\ \mathbf{F}_R & 0 \geq S_R \end{cases} \quad (17)$$

185 in which $S_L = u_L - q_L \sqrt{gh_L}$, $S_* = u_*$ and $S_R = u_R + q_R \sqrt{gh_R}$. Besides, the accuracy of
 186 numerical scheme is further improved by applying the WAF TVD algorithm on the FV
 187 surface for flux computations.

188

189 (5) Last step: Finally, the FEM solution procedure is applied again to solve the sediment
 190 transport equation and bed deformation equation as below (more detailed derivations can be
 191 referred to Chen et al. (2011))

$$192 \quad \mathbf{S}^{n+1} = \mathbf{S}^n - \mathbf{M}^{-1} \Delta t (\mathbf{C}\mathbf{S} + \mathbf{K}_m \mathbf{S} - \mathbf{f})^n + \mathbf{M}^{-1} (\Delta t)^2 (\mathbf{K}_s \mathbf{S} + \mathbf{f}_s)^n \quad (18)$$

$$193 \quad z_b^{n+1} = z_b^n - \frac{1}{1 - \xi} (\mathbf{H}\mathbf{q}_b + \mathbf{f}_c) \quad (19)$$

194

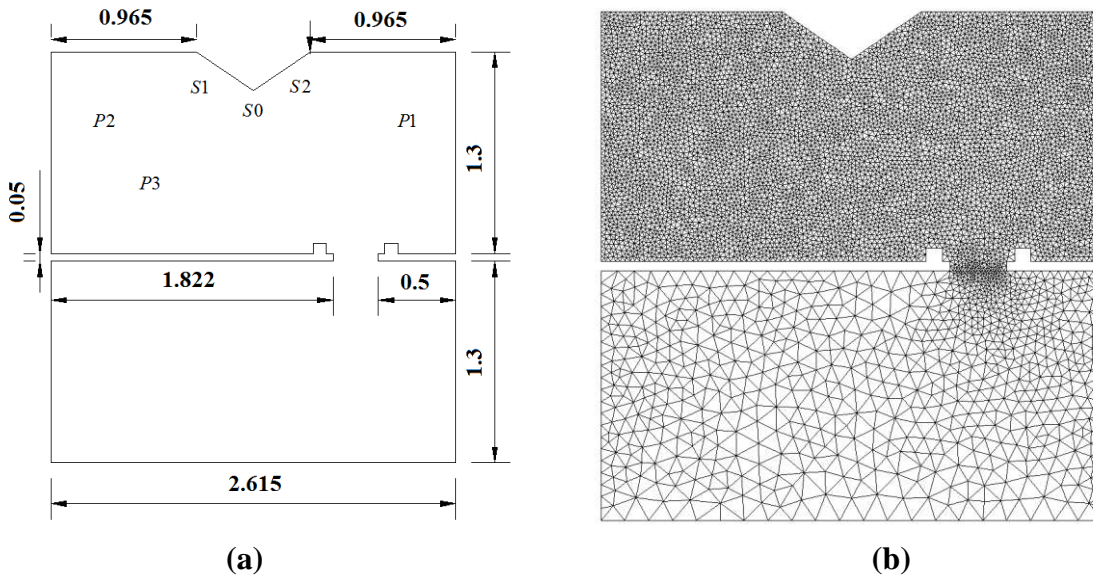
195 4. Model Verifications

196

197 4.1 Flood flow in a horizontal 2-D water tank

198

199 This model test is based on the benchmark unsteady flow experiment carried out in the
 200 Spanish CITEEC laboratory by J. Puertas (Brufau et al., 2004). The computational domain is
 201 composed of two rectangular water tanks, which are connected by a sluice gate and the rest
 202 parts are solid walls. The upstream tank contains reservoir water and the downstream tank is
 203 the flooded area, which also has a triangular barrier placed on one side of the wall to generate
 204 complex geometry and flow conditions. The bed roughness of the whole computational
 205 domain is $n = 0.018$. The initial water depth in the upstream tank is 0.5 m, as compared with
 206 0.1 m in the downstream area. The lift of the sluice gate is assumed to be instantaneous. Here
 207 we will use the numerical simulations to reproduce the unsteady flooding process. The
 208 general layout of the computational domain with the location of six measurement points and
 209 the computational meshes are shown in Fig. 1 (a) and (b), respectively.
 210



212

213

214

215

216

217

Fig. 1 Flood simulation in a horizontal 2-D tank. (a) Domain layout and measurement points; (b) Computational meshes

218

219

220

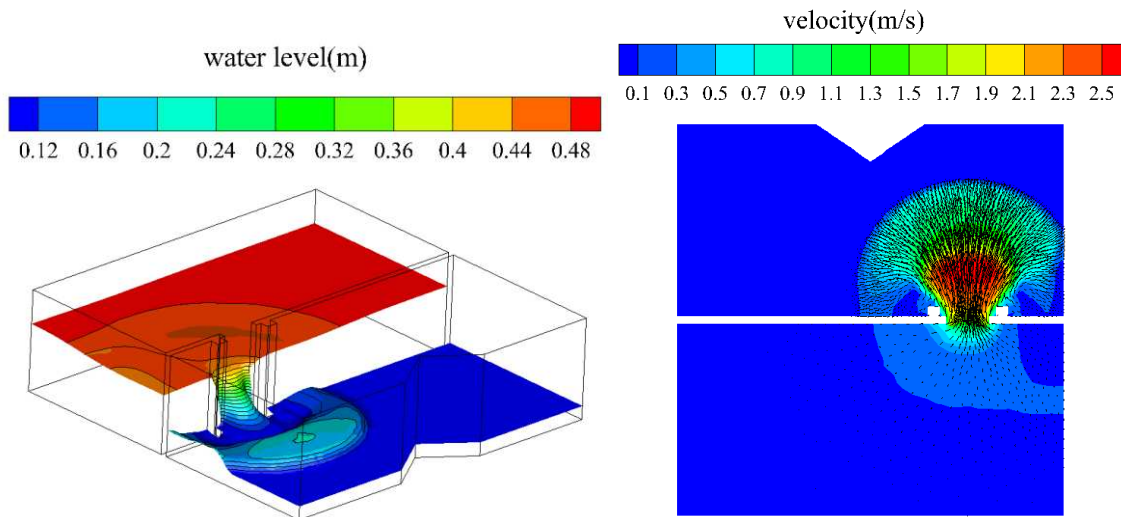
221

222

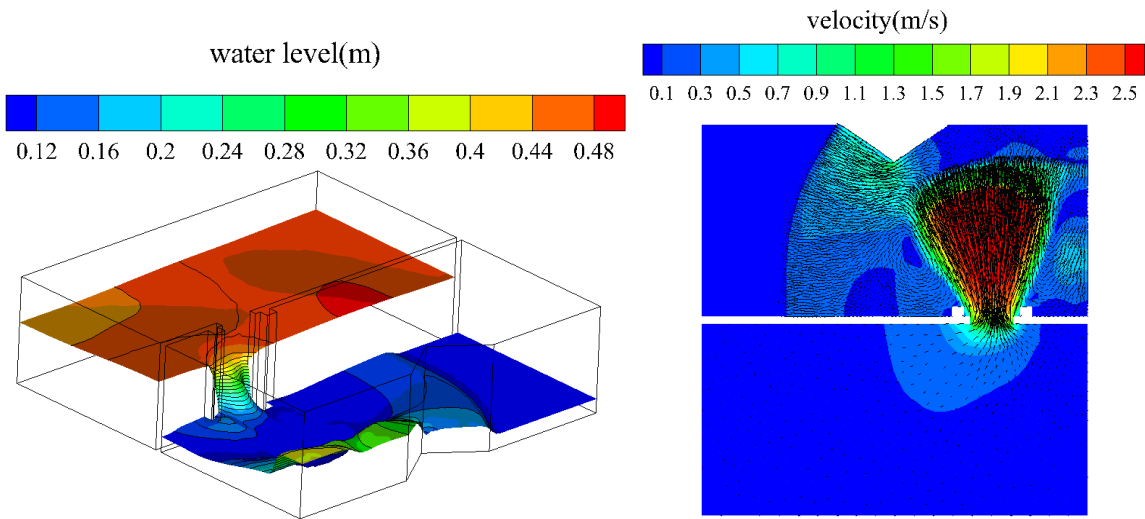
223

224

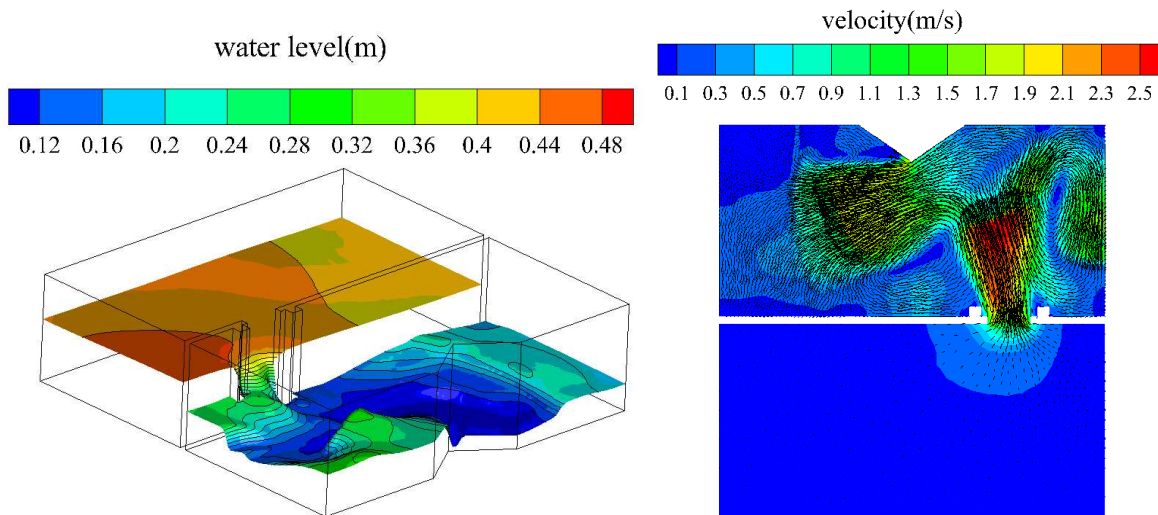
Based on the numerical simulations, the computed water surfaces and velocity fields of the unsteady flood flow are shown in Fig. 2 at four different time instants, at $t = 1, 2, 4$ and 8 s, respectively. The simulations showed that the dam break flows quickly propagated to the downstream region and the flood route was altered due to the existence of the triangular barrier. This subsequently generated a large circulation zone arising from the flow-solid wall interactions. Here the capability of the hybrid FEM-FVM model to reproduce complex flood flow patterns has been demonstrated.



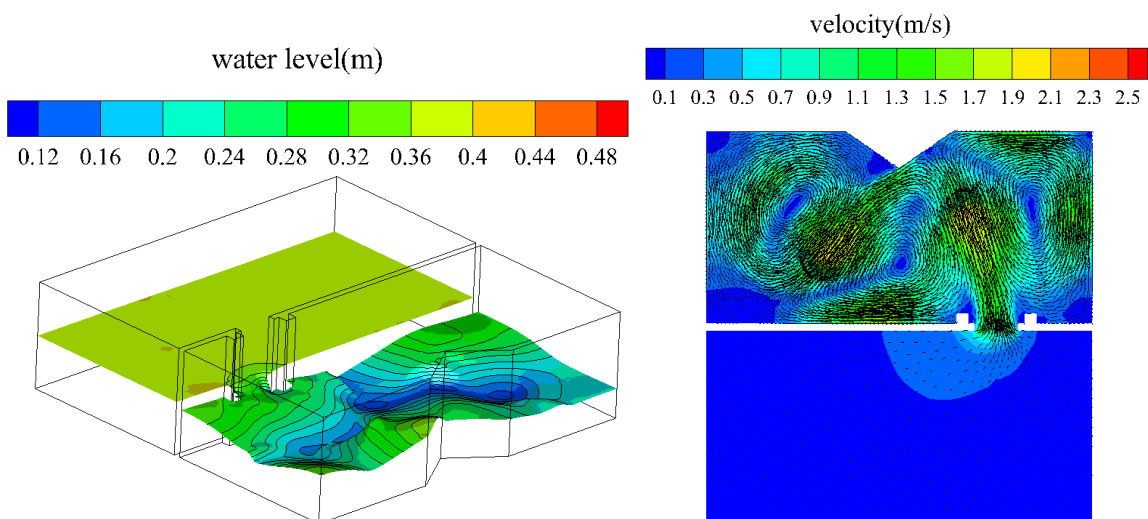
225



226
227



228



229
230
231

232 **Fig. 2 Computed water surface (left column) and velocity (right column) contours of**
233 **flood flow in a horizontal 2-D tank at $t = 1, 2, 4$ and 8 s (from up to down)**

234 To quantitatively validate the accuracy of numerical modeling, the computed time-dependent
 235 water surface levels at six measurement points (as shown in Fig. 1) are shown in Fig. 3, and
 236 compared with the experimental data of Brufau et al. (2004). The comparisons indicated that
 237 the general agreement is quite satisfactory and the numerical model is able to predict the
 238 unsteady flood flow propagation and interaction with the triangular obstacle. Meanwhile, the
 239 location and amplitude of the shock waves are also well captured.

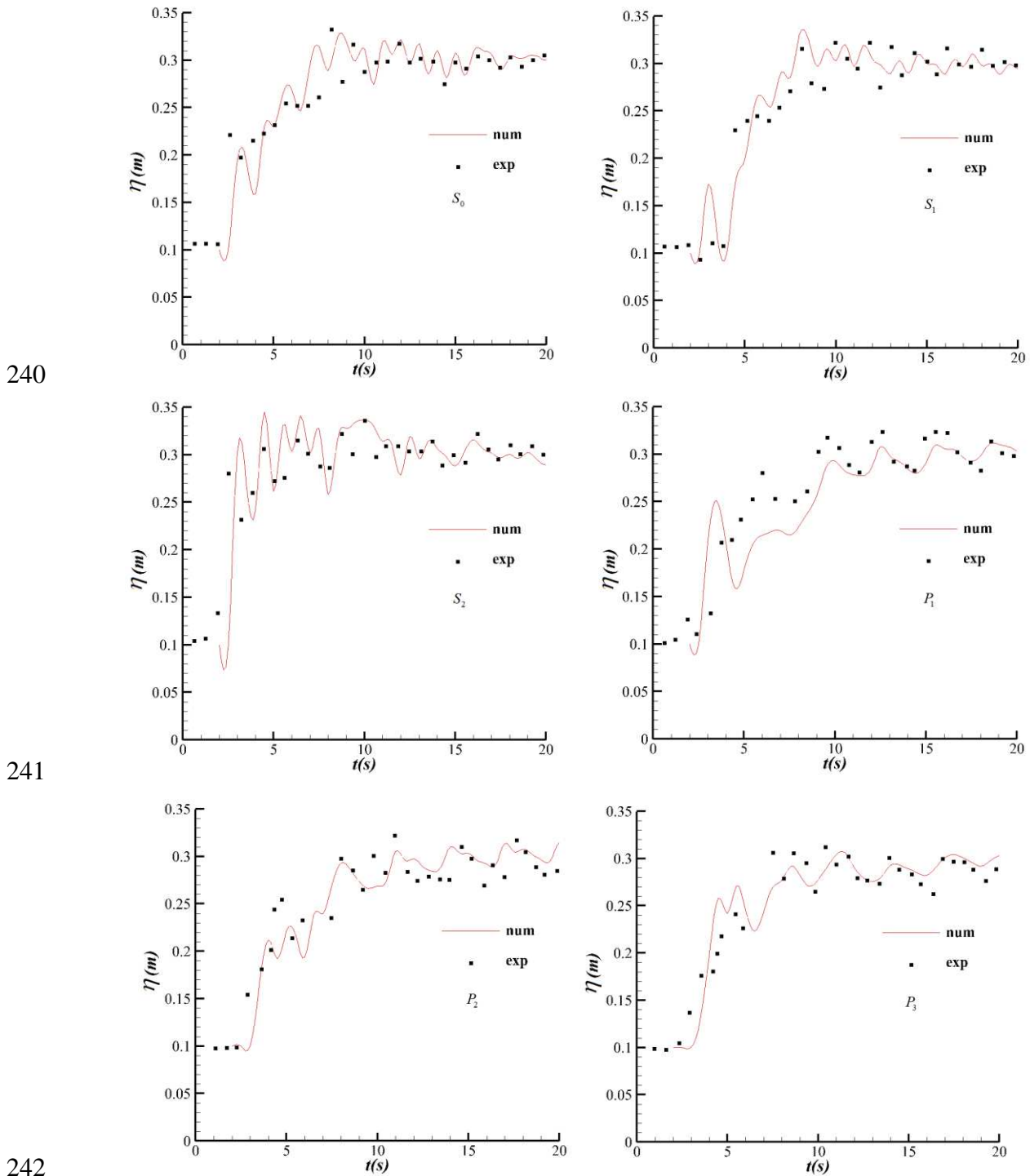
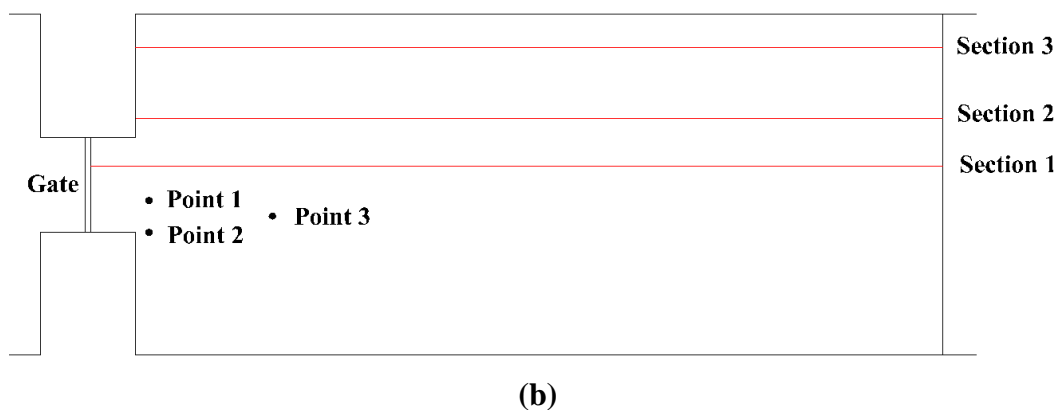
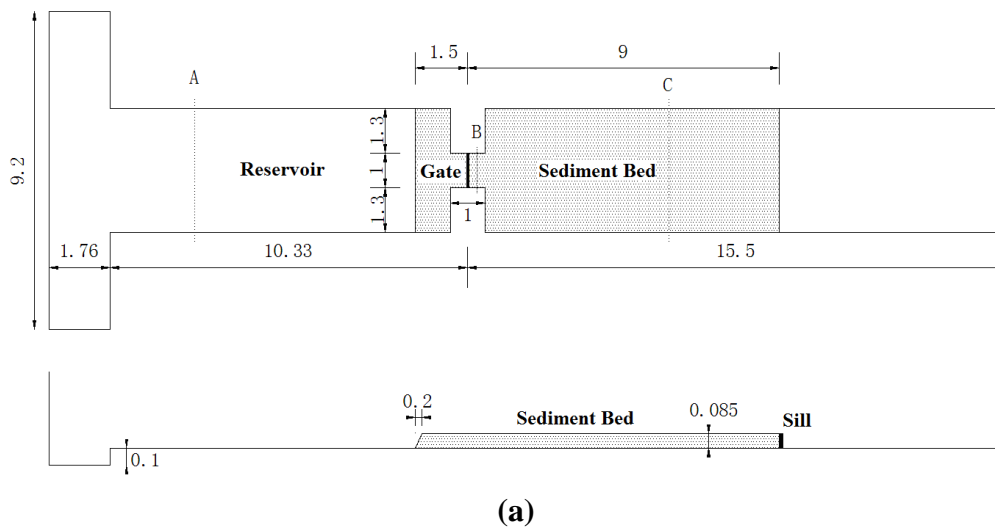


Fig. 3 Time history of computed (lines) and measured (dots) water surface levels of unsteady flood flow at measurement points $S_0, S_1, S_2, P_1, P_2, P_3$

245 **4.2 Dam break flow over a mobile bed channel**

246

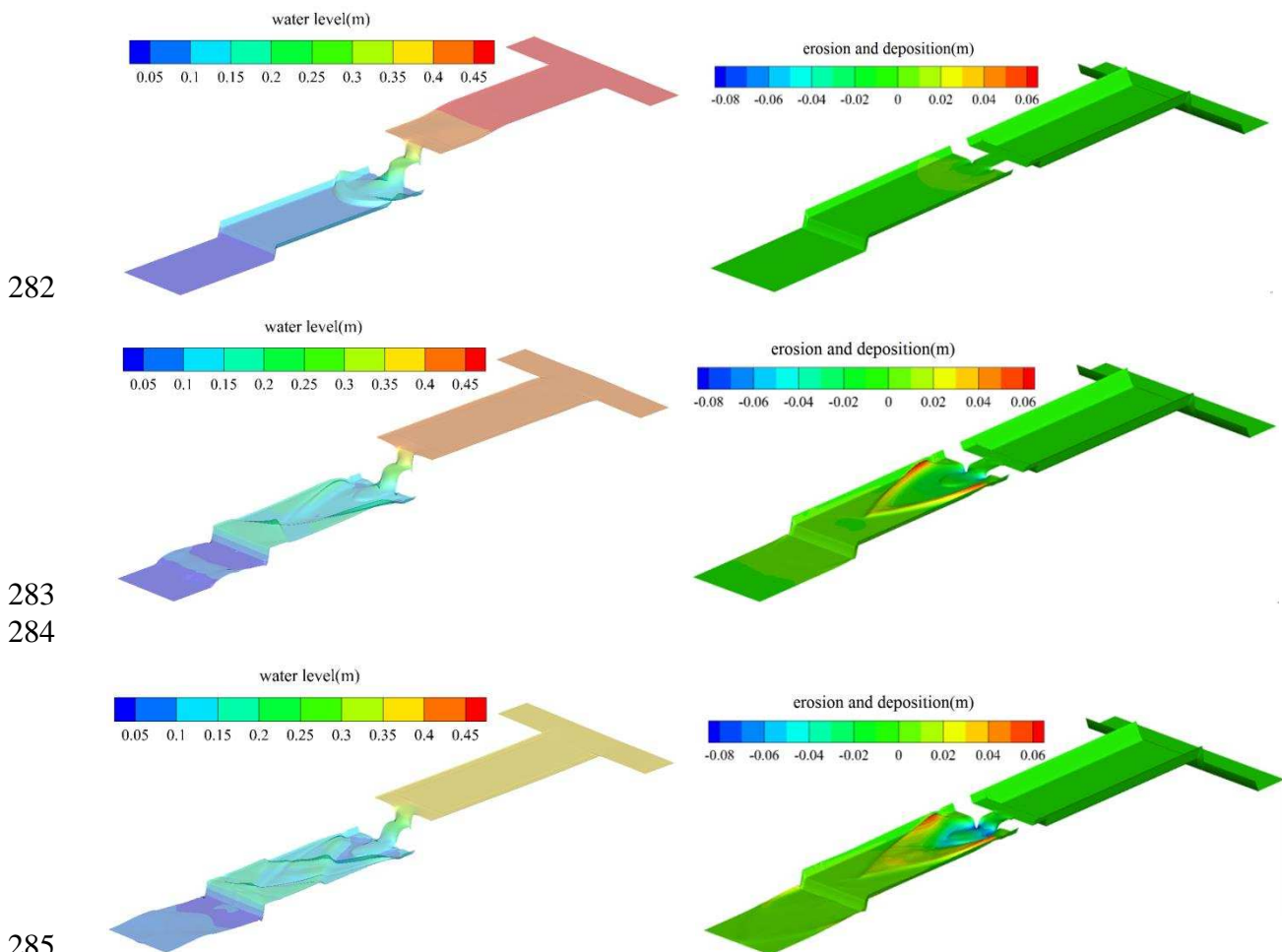
247 In this section, we use the proposed hybrid FEM-FVM model to reproduce a laboratory
 248 experiment of mobile bed dam break flow carried out in the Hydraulics Unit of the LEMSC,
 249 Catholic University of Louvain (Soares-Frazao et al., 2012). The computational domain is 27
 250 m long, the width of upstream and downstream channels is 3.6 m and a sluice gate is placed
 251 in the middle of the channel connection. The thickness of sediment layer is 0.085 m, which
 252 extends 1.5 m in the upstream side and 9.0 m in the downstream side. The mean diameter of
 253 sediment material is $d_{50} = 1.61$ mm, relative density $\rho_s / \rho_w = 2.63$, and bed porosity $\xi =$
 254 0.42. The roughness is $n = 0.0165$ for the sediment bed and $n = 0.01$ for the fixed bed. The
 255 initial water depth in the upstream reservoir is 0.47 m and the downstream channel is dry. The
 256 dam break was assumed to occur instantly and the subsequent flood process lasted for 20 s. A
 257 schematic setup of the computational domain is shown in Fig. 4(a). To validate the numerical
 258 simulations, three measurement points and measurement profiles in the longitudinal direction
 259 of the channel are taken in the computational domain as shown in Fig. 4(b).



264 **Fig. 4 (a) Schematic setup of computational domain for mobile bed dam break flow**
 265 **(unit in meter); (b) Locations of measuring points and profiles**

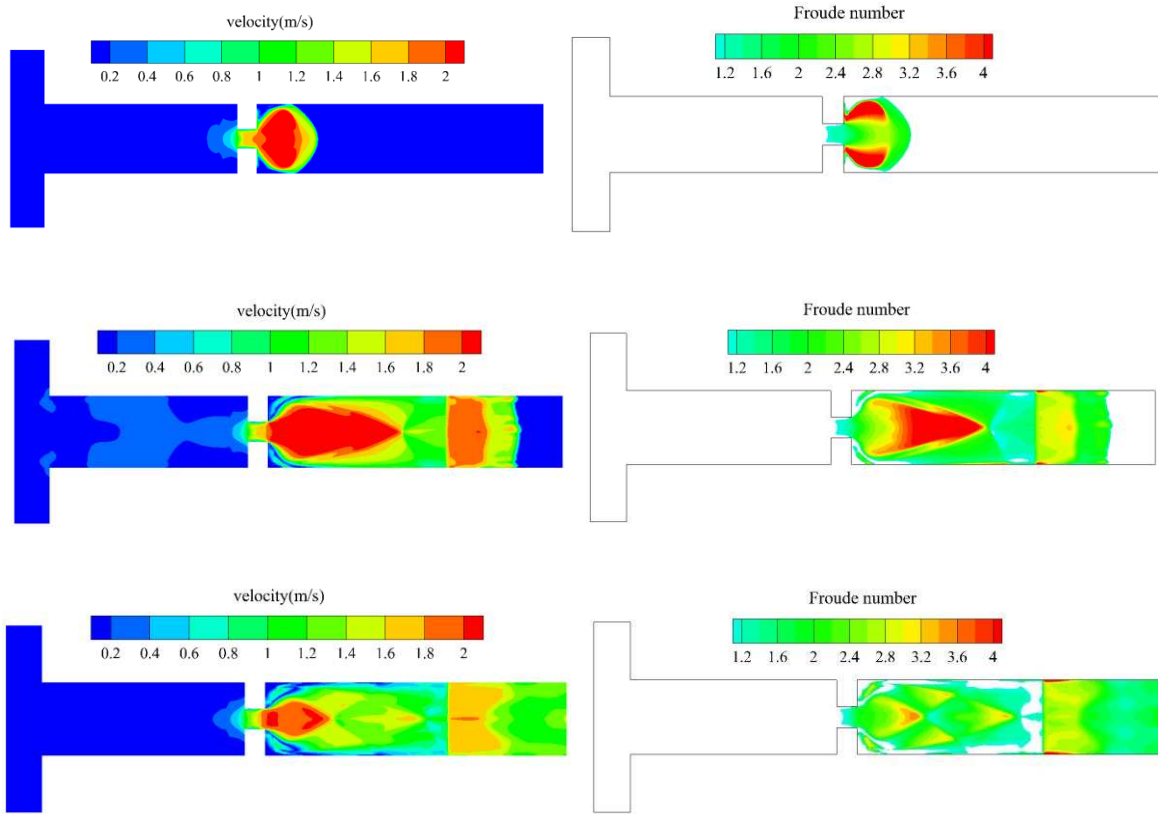
266

267 The computed water surface levels and sediment bed deformations are shown in Fig. 5, and
 268 the velocity fields and flow Fr numbers are shown in Fig. 6, respectively, at three selected
 269 times at $t = 2.0, 8.0$ and 20.0 s, respectively. The erosion and deposition results in Fig. 5
 270 indicated that as the dam break flow propagated over the mobile bed it caused severe erosion
 271 at the original dam site. Later on, with the change of local flow and bed conditions the dam
 272 break flow reduced its capacity and deposited the sediment materials in the downstream area,
 273 forming something like an alluvial fan. Besides, the water surface contours showed the
 274 generation and evolution of strong dam break shock waves propagating in the downstream
 275 direction, which led to irregular wavy water surfaces. Generally speaking, the dam break flow
 276 could generate significant sediment erosions and depositions in a very short period of time
 277 and thus constitute a rapid alluvial process. For example, the sediment bed layer at the dam
 278 site was nearly eradicated at time $t = 8$ s after the dam break, and the maximum deposition
 279 height added up to 7 cm around $t = 20$ s. As a result, a total of around 14 cm topographic
 280 difference in the original flat bed was generated within a short time scale.
 281



285
 286
 287
 288 **Fig. 5 Computed water surface (left column) and sediment bed deformation (right**
 289 **column) contours of mobile bed dam break flow at $t = 2, 8$ and 20 s (from up to down)**

290
291



292
293

294
295

296
297

298 **Fig. 6 Computed flow velocity (left column) and Fr number (right column) contours of**
299 **mobile bed dam break flow at $t = 2, 8$ and 20 s (from up to down)**

300

301 The velocity fields in Fig. 6 show that in the early stage of dam break, the high velocity area
302 concentrates near the dam site, but it spreads out along the centreline of the channel as time
303 goes on and the flow intensity also tends to decrease. The mobile sediment layer has an
304 obvious effect on the dam break process and acts as a buffer zone to reduce the flow velocity,
305 which is demonstrated by the fact that the velocity in the fixed bed portion of the channel as
306 shown at time $t = 8$ s is larger than that in the sediment channel in the cross-sectional area.
307 Besides, the Froude number contours have also showed a similar trend. Although the flow
308 regime is supercritical in most of the downstream areas, the flow intensity becomes smaller
309 and more uniformly distributed at the later stage of dam break process.

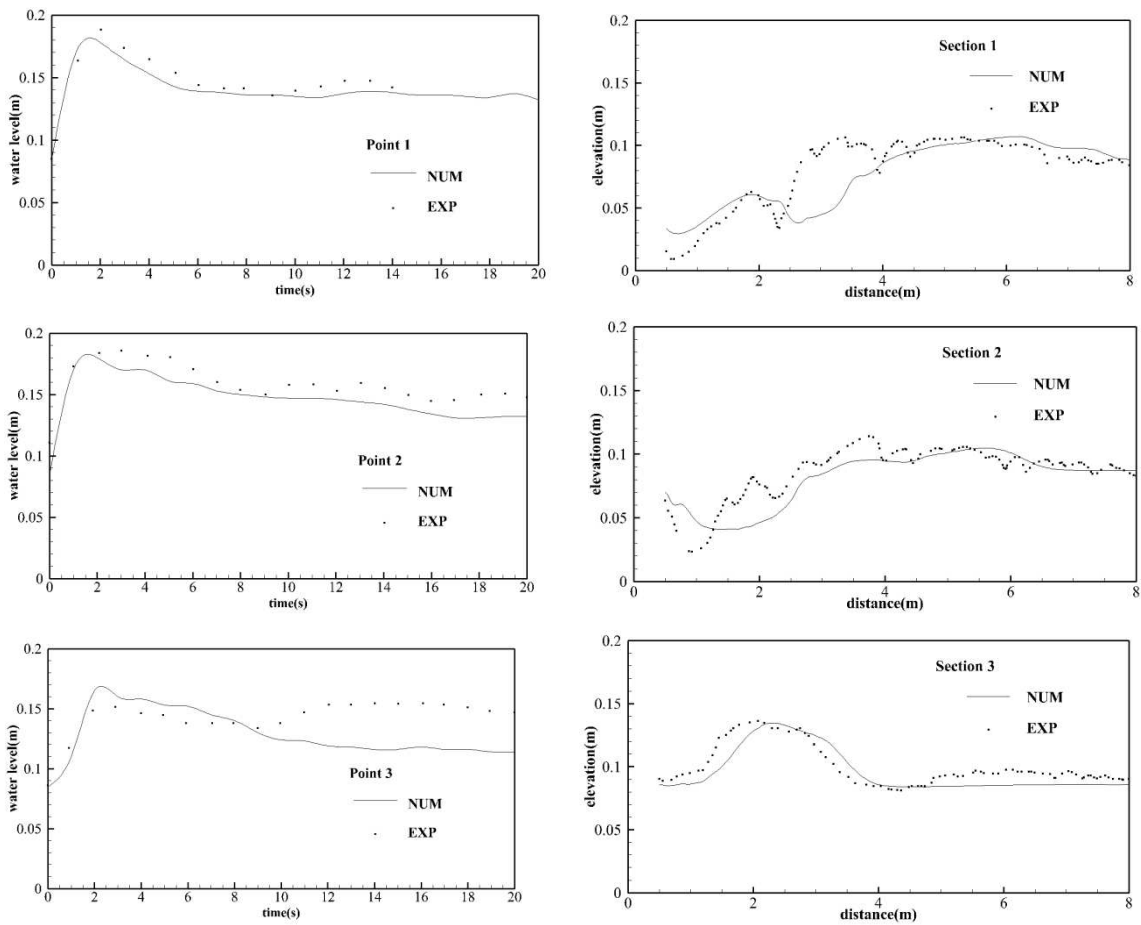
310

311 The comparisons between the simulated and measured water surfaces as well as sediment bed
312 elevations are shown in Fig. 7. Generally speaking, the agreement between the numerical
313 simulations and experimental measurements is quite satisfactory in the engineering interest by
314 considering the complex water-sediment interactions and efficient simulation time of the
315 model using a hybrid FEM-FVM solution scheme. However, relatively larger errors can be
316 found for the measuring point 3 and section 1, which is due to the correlation of

317 computational errors between the water surface level and bed deformation.

318

319



320

321

322

323

324 **Fig. 7 Measured and computed water surface levels (left column) and sediment bed**
325 **elevations (right column)**

326

327

328 4.3 Morphological modelling of dam removal experiment

329

330 To validate the numerical model in the prediction of morphological changes at the dam site
331 area, the benchmark laboratory experiment of Cantelli et al. (2004) is used. The original work
332 reported on the erosion of a deltaic front induced by the removal of a dam. The installation of
333 a dam on the river induces sedimentation at the upstream end of the reservoir. The removal of
334 a dam causes erosion into the resulting deposit and subsequent disastrous sediment flows. Not
335 many numerical models have been developed to model such a complex process including the
336 erosion, transport and deposition of sediment due to the difficulties in treating the steep
337 streamwise bed slope created by the dam removal that induces high flow velocities and
338 sediment transport rates, and the variations in the width of the channel incising into the
339 deposit.

340

341 According to Cantelli et al. (2004), the experiments were performed at St. Anthony Falls
342 Laboratory, University of Minnesota. A rectangular glass-walled flume 14 m long, 0.61 m
343 wide and 0.48 m high was modified to model a long reservoir of uniform width. The initial
344 slope of the sediment bed was 1.8%. The dam was located 9 m from the inlet of the flume. To
345 simplify the problem, non-cohesive sediment was used in the experiment. Ten runs using
346 different water flow discharges and dam removal procedures were considered in the
347 experiment and we reproduce Run 6, which is an instantaneous collapse.

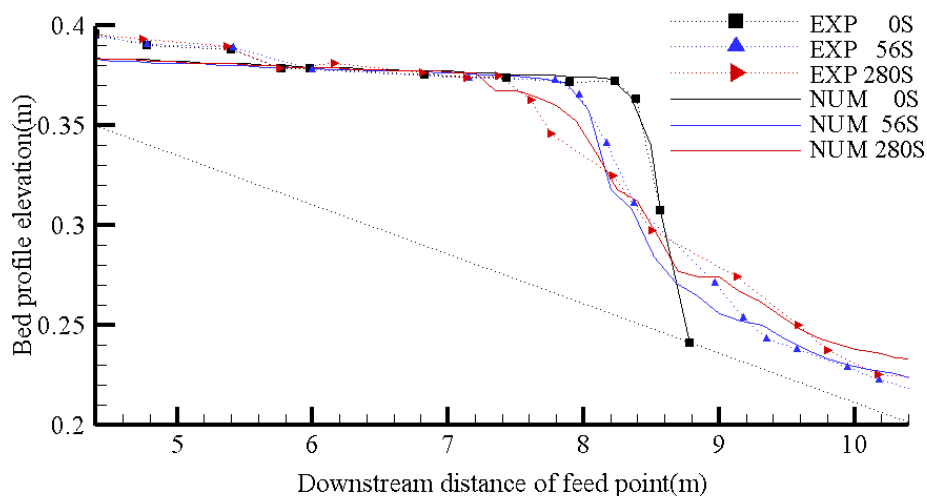
348

349 The model simulation time duration is 5600 s, which is set to be consistent with the physical
350 experiment (Cantelli et al., 2004). The numerical domain is 14 m long and 0.61 m wide. Non-
351 structured grids were used with 29518 nodes and 57570 grids. The roughness of the channel
352 bed was taken as 0.016. Computational time step was automatically adjusted based on a CFL
353 condition of 0.4. The flow discharge rate is $Q = 0.3 \times 10^{-3} \text{ m}^3/\text{s}$ and the sediment grain size is
354 $D_{50} = 0.8 \text{ mm}$.

355

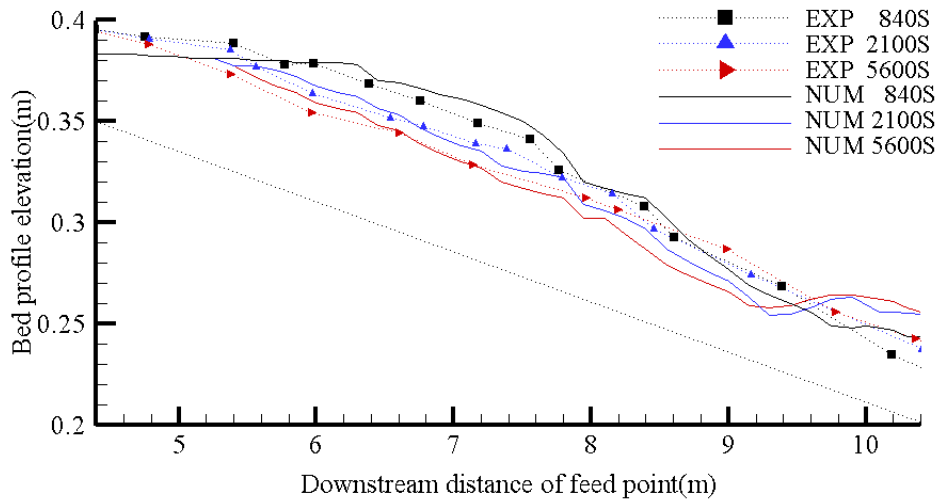
356 Fig. 8 shows the evolutions of the bed profiles along the channel center during the erosion of
357 the reservoir deposits at different time instants. The erosion upstream of the deposit front and
358 the deposition downstream are clearly visible. The dotted line in the figure represents the
359 initial bed profile. It shows that after the sudden removal of the dam, the flow incises into the
360 reservoir deposit, first rapidly and then more slowly. Towards the end of model simulation
361 around time $t = 5600 \text{ s}$, the equilibrium bed slope is approximately equal to the initial slope
362 value. A very good agreement in the morphological profiles has been found between the
363 numerical simulations and measurement data of Cantelli et al. (2004) in Fig. 8. Slightly large
364 discrepancies only appear at $t = 5600 \text{ s}$ near the far downstream side of the deposit, which is
365 probably due to the numerical parameter uncertainties after the long-time simulation.

366



367

368

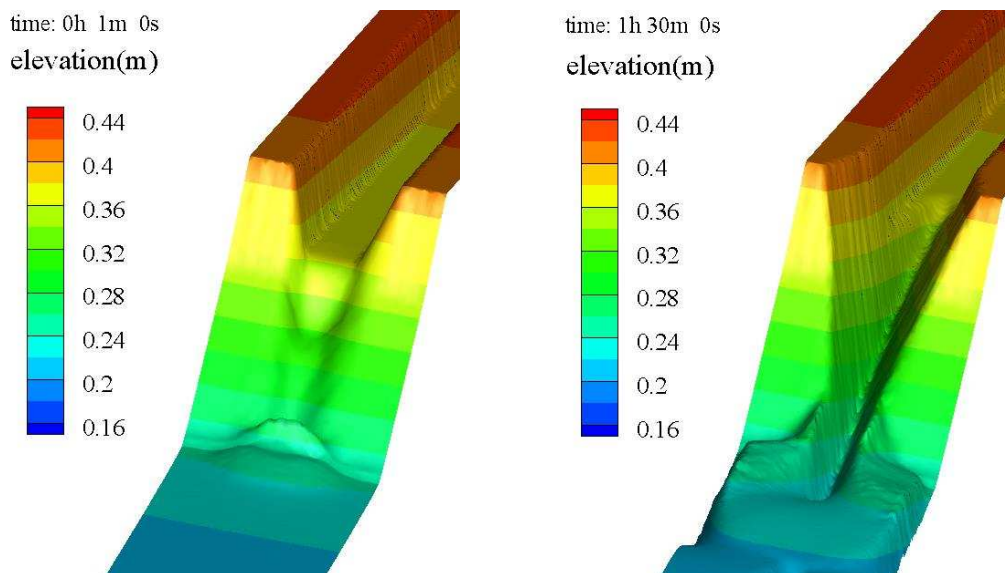


369
370

371 **Fig. 8 Computed and measured time-evolution of bed profiles along the channel center**
 372 **(Dam located 9 m downstream of the feed point and flow from left to right, following**
 373 **Cantelli et al., 2004)**
 374

375 Furthermore, the computed 3D longitudinal channel profiles are shown in Fig. 9, for the time
 376 instants at $t = 1$ min and 1.5 hour, respectively, after the erosion started. It clearly
 377 demonstrated the spatial and temporal variations of the incision and widening of the channel.
 378 The so-called erosional narrowing as found by Cantelli et al. (2004) in their laboratory
 379 experiment was also found in the present numerical simulations.

380
381



382
383
384

385 **Fig. 9 Three-dimensional longitudinal profiles of channel erosion process**
 386

387 **5. Model Applications in Field Case Study**

388

389 **5.1 Sediment-laden flood flow at Polo Hydropower Plant**

390

391 The Polo Hydropower Plant is located at the two river confluence in the Yi Autonomous
392 Region of Sichuan Province, which was put into operation in December 1999. During the
393 heavy rainstorms of July 28, 2001, the sediment-laden floods from the two rivers inundated
394 the power plant. The situation was further deteriorated by the large quantities of sediment
395 deposition, which raised the river bed by about 5 ~ 7 m. The two rivers near the confluence
396 region demonstrated mountainous river features with relatively steep bed slope. The flow
397 regime was quite complicated due to the drastic changes of topographic and boundary
398 conditions. To re-investigate this natural disaster and provide useful information for the
399 engineering practice in future, in this study we carry out both the physical experiment and
400 numerical simulation to reproduce the flood and sediment transport process near the river
401 confluence. The physical experiment was carried out at the State Key Laboratory of
402 Hydraulics and Mountain River Engineering, Sichuan University.

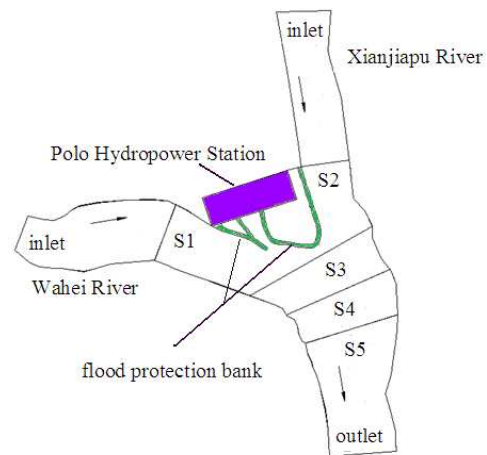
403

404 The topographic data of the site were obtained from the field survey carried out two years
405 before the 2001 sediment-laden flood disaster. The field photo of the original Polo
406 Hydropower Plant and a schematic layout of the nearby rivers are shown in Fig. 10 (a) and
407 (b), respectively. The detailed river systems are introduced as follows: The upstream flow
408 inlet of one tributary river, which is called the Wahei River, is 250 m away from the
409 confluence junction. The upstream inlet of another tributary river, called the Xianjiapu River,
410 is 200 m away. The downstream flow outlet is 150 m away from the confluence point. For a
411 comparison, the field photos of the hydropower plant after being damaged by the flood and
412 sediment flows in July 2001 are shown in Fig. 11 (a) and (b).

413



(a)



(b)

414

415

416

417 **Fig. 10 (a) Field photo of original Polo Hydropower Plant; (b) Schematic layout of rivers**



419

420

421

422 **Fig. 11 Field photo of damaged Polo Hydropower Plant caused by (a) Flood flows; (b)**
 423 **Sediment deposits**

424

425 5.1.1 Modeling parameters

426

427 The detailed modeling conditions are taken as follows. Due to the lack of real time
 428 observations of flow and sediment hydrographs during the flood event, here we simply use
 429 the peak flow discharges of the July 28 flood as input parameters for the present physical and
 430 numerical models. That is to say, we assume the Wahei River has a flow discharge of 1350
 431 m^3/s ($P = 2\%$) and Xianjiapu River has a flow discharge of 712 m^3/s ($P = 5\%$). The sediment
 432 concentration is assumed to be in saturation at the upstream river inlets and the free outflow
 433 boundary conditions are imposed at the downstream flow outlet. The gradation of the
 434 sediment materials is shown in Table 1.

435

436

437 **Table 1. Gradation of sediment materials at upstream inlet**

Diameter (mm)	>500	500-200	200-60	60-20	20-5	5-2	2-0.5	0.5-0.25	<0.25
Percentage (%)	0.0	28.8	10.5	18.7	16.8	17.3	6.1	1.0	0.8

438

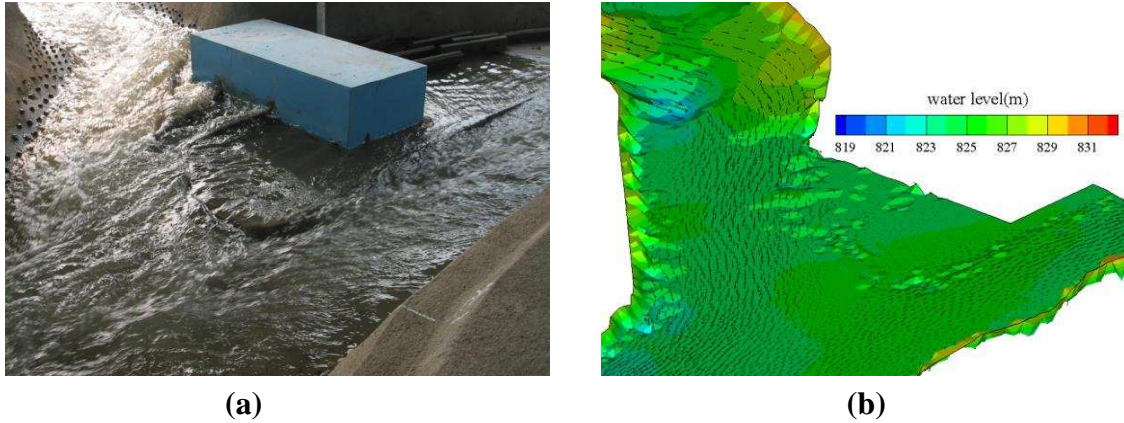
439

440 5.1.2 Flood flow simulation results and analysis

441

442 In the first phase of the study, we carried out physical experiment and numerical simulations
 443 for the water flow only without considering the sediment transport. Fig. 12 (a) and (b) shows
 444 the inundation of the hydropower plant due to the confluence of flood water from the two
 445 river tributaries. The physical experimental photo in Fig. 12 (a) and the numerical water level
 446 in Fig. 12 (b) are qualitatively compared together and it shows that the two converging rivers
 447 caused significant flooding damages to the hydropower plant.

448

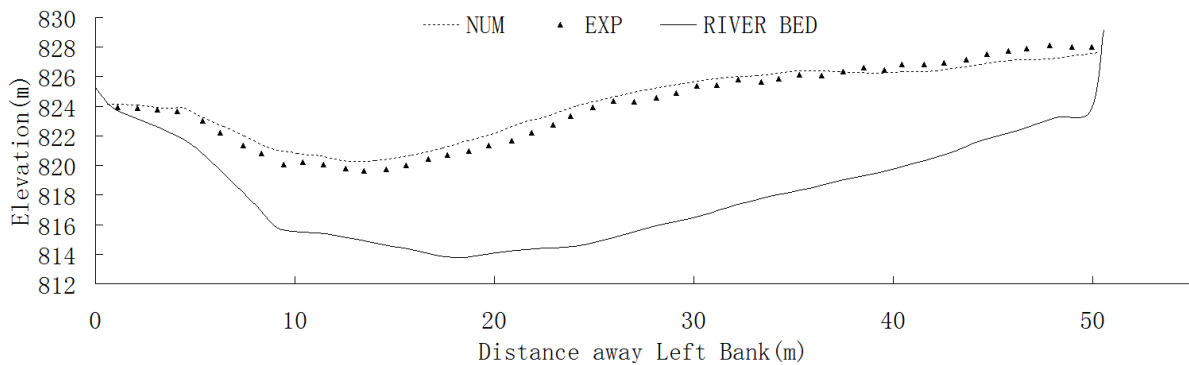


449
450
451

Fig. 12 Flood inundation of the hydropower plant due to river confluence. (a) Physical experiment; (b) Numerical simulation

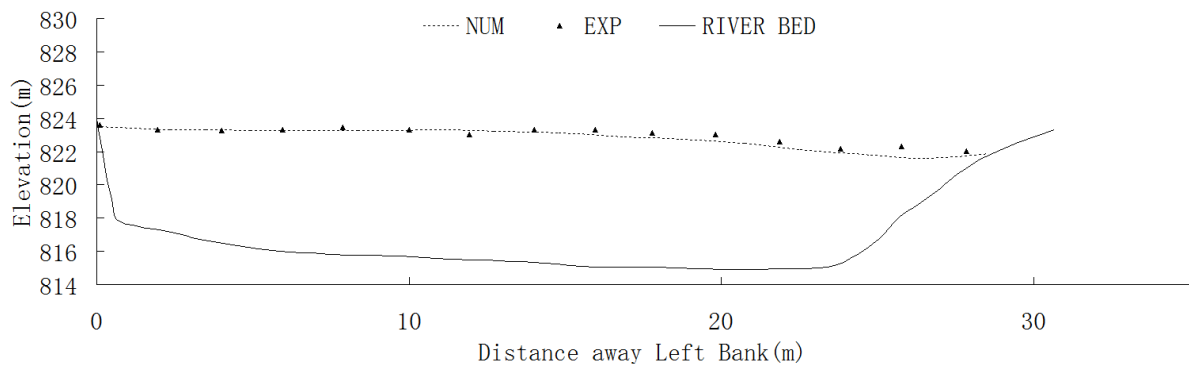
454

455 To further investigate the flood flow features, the water surface profiles at two measurement
456 sections S1 and S2 (as shown in Fig. 10 (b)) are compared between the numerical results and
457 experimental data in Fig. 13 (a) and (b), respectively. Besides, the computed flow velocity
458 field and its good agreement with the experimental measurement are shown in Fig. 14 (a) and
459 (b).



460
461

(a)



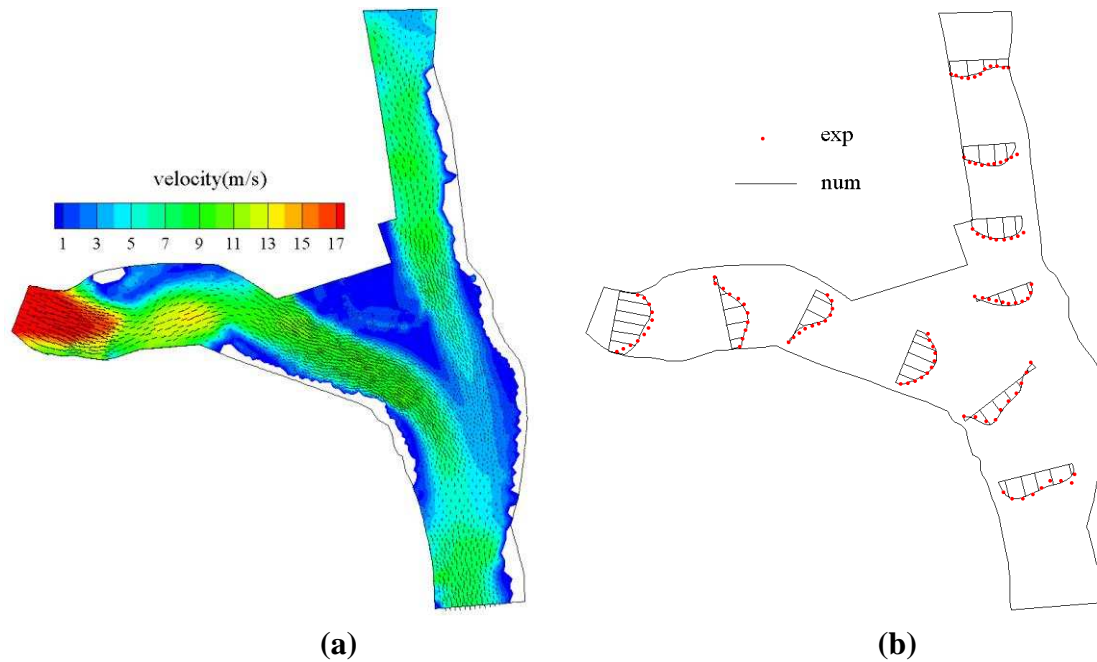
462
463
464

(b)

Fig. 13 Computed and measured water surface profiles in cross-sectional area at measurement sections (a) S1; (b) S2

466

467
468



469
470
471
472
473
474

Fig. 14 (a) Computed velocity field; (b) Comparisons of experimental and numerical velocities near the river confluence area

475 It can be seen from Figs. 13 and 14 that the inundation of the hydropower plant was caused
476 by two different flood scenarios: (1) As the tributary river - Wahei River has relatively steep
477 bed slope, irregular channel cross-section and meandering flow pattern, the direct flow thrust
478 and deflection of this river caused the flood water to overtop over the protection bank. This
479 can be easily understood through Fig. 13 (a) for the cross-sectional water level at Section S1,
480 where there exists a large difference in the water surface levels of about 7.45 m. (2) On the
481 other hand, another tributary river - Xianjiapu River inundated the hydropower plant due to
482 the flood water from the two tributary rivers running against each other. The interaction of the
483 two rivers reduced the local flow velocity and accordingly increased the flow depth, resulting
484 in the water level being higher than the protection bank. This can be partly demonstrated by
485 the cross-sectional water level in Fig. 13 (b) at measuring section S2, as well as the flow
486 velocity field near the confluence area in Fig. 14. Besides, in both Figs. 13 and 14 the
487 numerical results agree quite well with the experimental data, indicating the accuracy of the
488 proposed FEM-FVM model in water flow simulations.

489
490

491 5.1.3 Sediment simulation results and analysis

492
493
494

In the second phase of the study, the physical experiment and numerical simulations for the mobile bed condition were carried out, based on the previous fixed bed works by feeding the

495 sediment materials into the river system at the upstream flow inlets. The aim is to investigate
496 the sediment transport and deposition process near the river confluence and evaluate its
497 influence on the inundation of the Polo Hydropower Plant. An illustrative photo of the
498 experimental site is shown in Fig. 15, which shows that the sediment deposition near the river
499 confluence also contributed to the damage of the power plant.

500
501

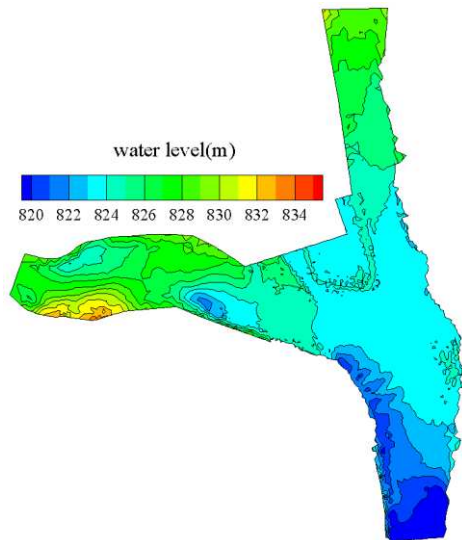
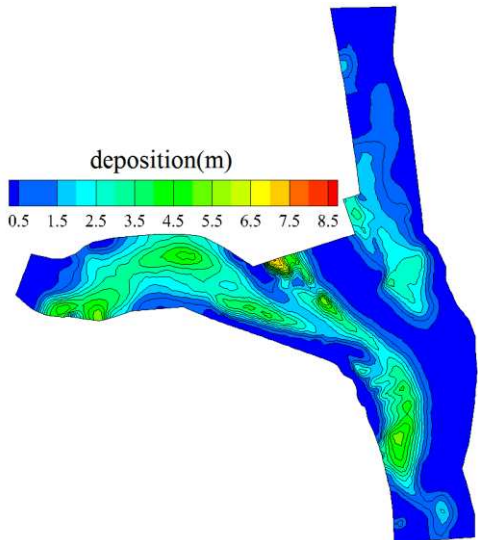


502
503
504
505
506

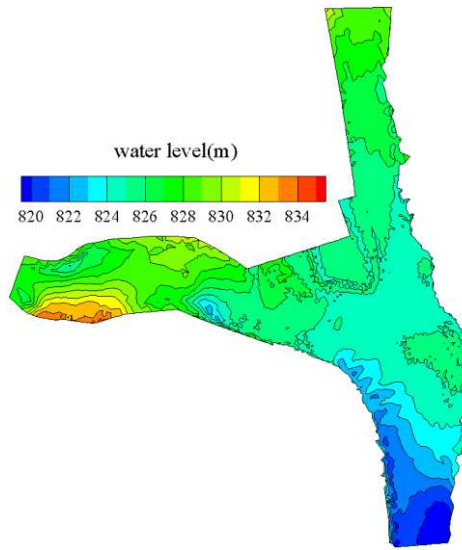
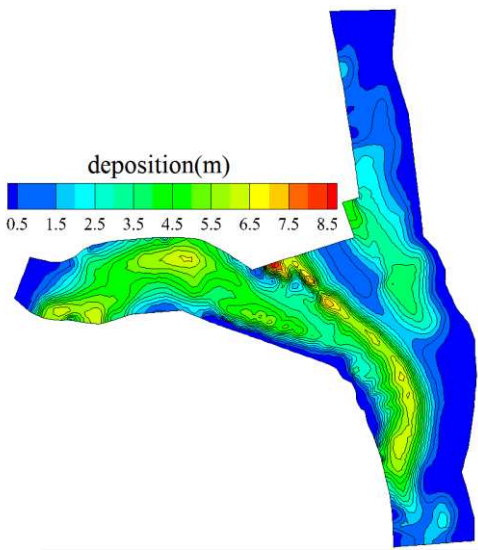
Fig. 15 Experimental photo of sediment deposition near the hydropower plant

507 Fig. 16 shows the sediment deposition thickness and water level contours at time $t = 1, 2, 4$
508 and 6 hr of the numerical simulations. The left column is the deposition layer thickness and
509 the right one is the water level. Fig. 16 demonstrates the importance of river confluence on
510 the sediment transport and deposition features, which contributed to the raising of river bed
511 and deteriorated the flood disasters. Due to the blocking effect of the Wahei River along the
512 Xianjiapu River's flow route, the sediment-laden capacity of the latter was greatly reduced,
513 leading to severe sedimentation of the river bed. On the other hand, due to that the upstream
514 sediment input of the Wahei River was very rich and the existing river training works blocked
515 part of the flow channel, the water surface slope in the confluence area was much smaller as
516 compared with its upstream value. This situation was made more serious by the two river
517 interactions, i.e. one river flowing against another as mentioned before. As a result, some
518 large sediment materials such as gravels were first deposited in the confluence region.
519 However, this deteriorated the situation by further reducing the local water surface slope and
520 caused more medium and even small sediment materials to be settled. Finally, the thickness
521 of the sediment deposits gradually exceeded the height limit of the river protection bank and
522 large quantities of the sediment materials were dumped into the hydropower plant.

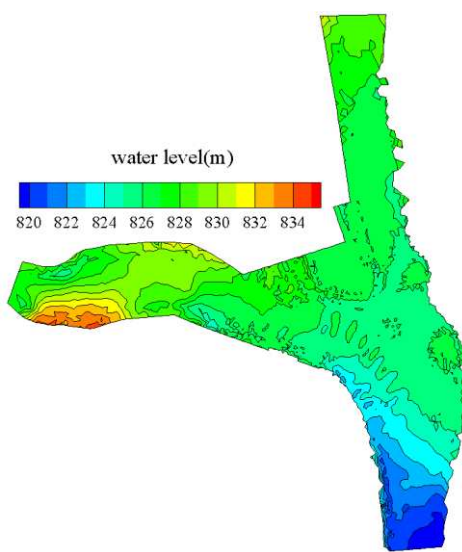
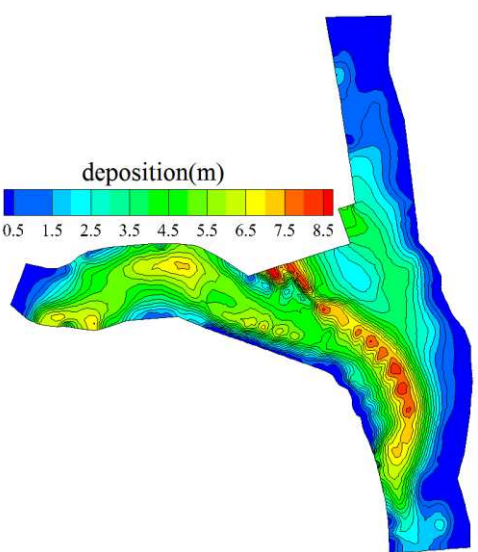
523



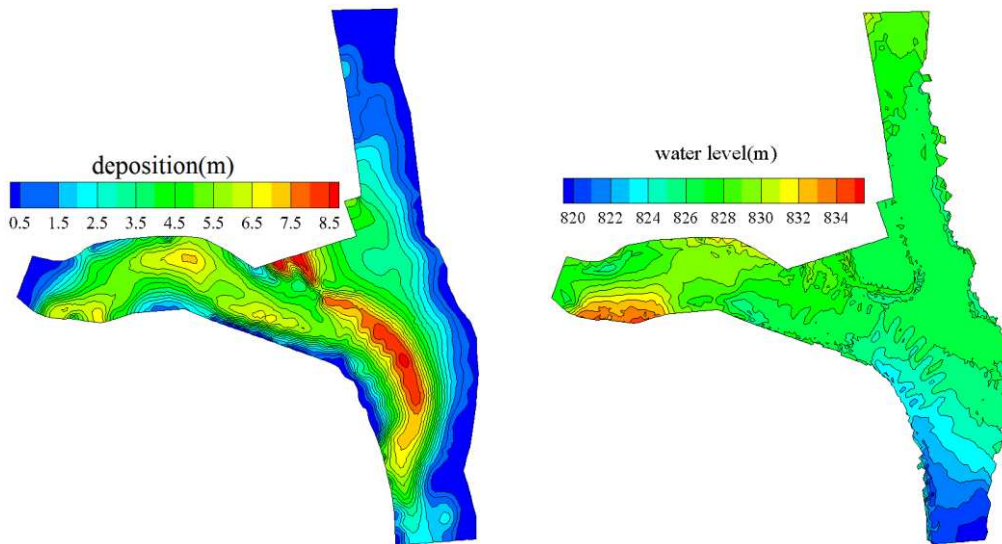
524
525



526
527



528
529

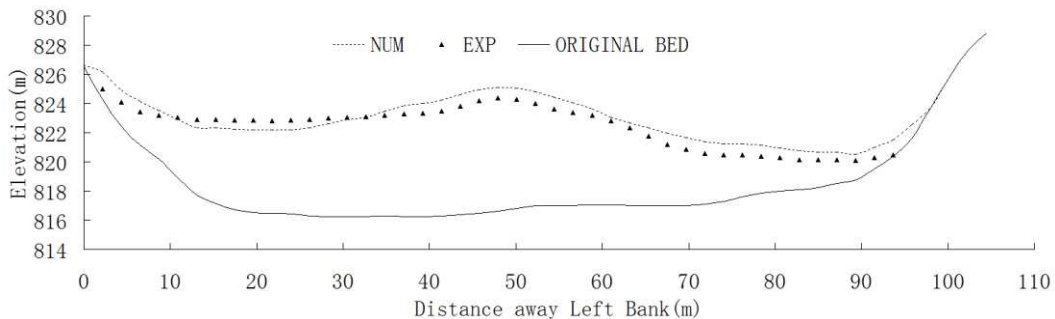


530
531
532
533
534
535

Fig. 16 Computed sediment deposition thickness (left column) and water surface level (right column) contours near river confluence at $t = 1, 2, 4$ and 6 hr (from up to down)

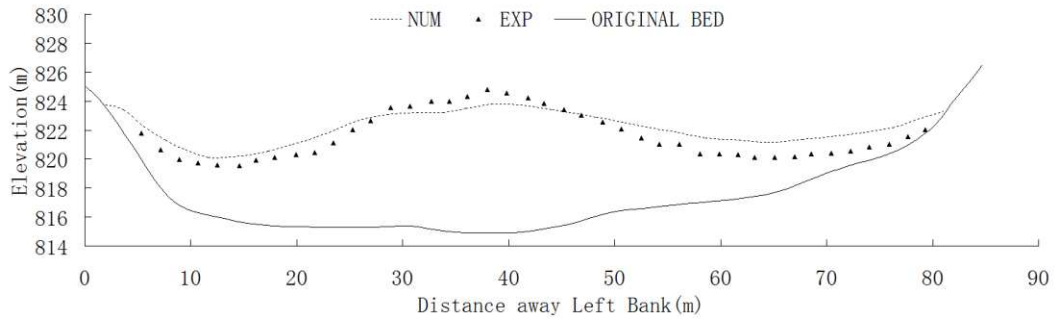
536
537
538
539
540
541
542
543
544
545
546
547

To quantitatively validate the accuracy of the numerical model for long time flow and sediment simulations, Fig. 17 (a) ~ (c) shows the computed and measured sediment bed profiles for the measurement sections S3 - S5 as shown in Fig. 10 (b). In spite of some discrepancies in the data set due to the complexity of the problem, the two results agree quite well in view of the engineering interest and it shows the numerical simulations realistically reproduced the sediment transport and deposition process during the two river confluence. According to the field observation records, large scale of landslides also happened during the storm flood and thus plenty of the debris stones were dumped into the power plant, with some gravel stones having diameter as large as 1.0 m. These have generated catastrophic effect on the damage of the building but they were difficult to model in either the physical experiment or numerical simulations.

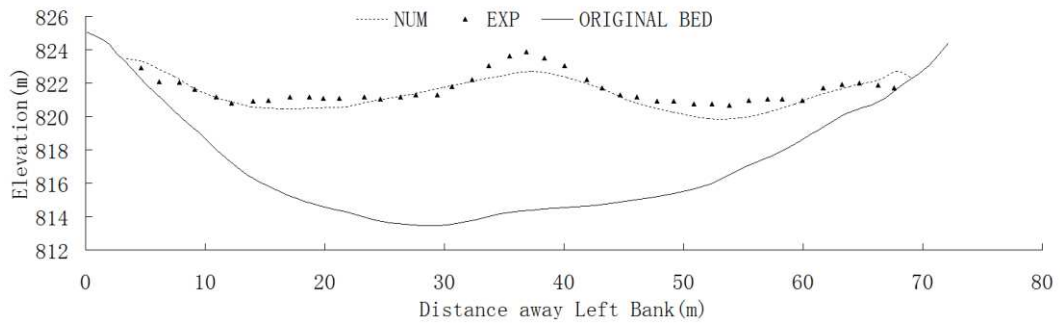


548
549

(a)



(b)



(c)

Fig. 17 Computed and measured sediment bed profiles in cross-sectional area at measuring sections (a) S3; (b) S4; (c) S5

The disagreement between the physical experiment and numerical simulations could be attributed to several reasons. Firstly, the simulation of mountainous rivers over relatively steep bed slope requires more stable numerical schemes, and some numerical treatments adopted in this paper could bring uncertainties and affect the simulation accuracy. Secondly, the present river systems have a bed slope around 0.04 and the characteristic sediment diameter is 35 mm, while the Meyer-Peter formula used in the FEM-FVM model only applies to the bed slope being less than 0.02 and sediment diameter being in the range of 0.4 ~ 29 mm. Lastly, the proposed numerical model uses the averaged horizontal velocities to compute the bed load transport. This approach did not adequately address the influence of secondary flows which are quite important in mountainous rivers.

577 **5.2 Tanjiashan Mountain 2013 Flood**

578

579 **5.2.1 Engineering background**

580

581 Tanjiashan Mountain Lake was formed during the Wenchuan Earthquake that happened in
582 May 12, 2008 and it is located 5 km upstream of the Old Town of Beichuan. The length of
583 the dam is 803 m along the river flow and the maximum cross-sectional width is 611 m. Due
584 to the adequate engineering works carried out after the Wenchuan Earthquake, the water level
585 in the lake reservoir has been maintained at a safety level of 713 m and the water storage
586 capacity is around 86 million m³. On July 9, 2013 the heavy precipitations in the catchment
587 area reached as large as 285 mm, which raised the water level of the Tanjiashan Lake by 8.0
588 m. As a result, the right portion of the dam was partially breached leading to a flood with
589 maximum discharge rate of 5000 m³/s. Subsequently, quite a few downstream areas were
590 inundated with the submergence depth exceeding 7.0 m. The damaged areas include some
591 heritage sites such as the Beichuan Hotel and Cemetery of Victims. Fig. 18 shows the site
592 photo of the flood and sediment inundation areas near Beichuan Hotel.

593



594

595

596 **Fig. 18 Site photo of flood and sediment (circled in red line) inundations near Beichuan**
597 **Hotel (<http://www.chinanews.com/shipin/2013/07-12/news251654.shtml>)**

598

599

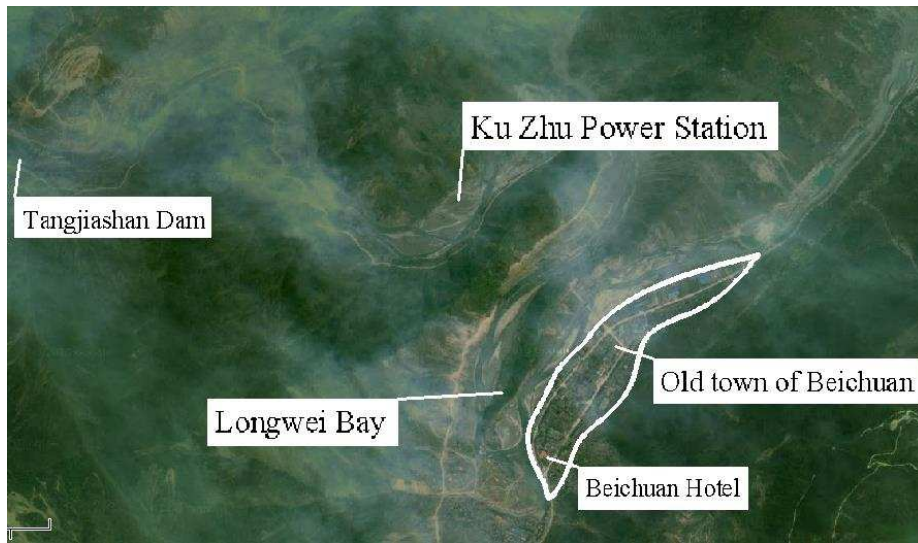
600 **5.2.2 Computational domain and model parameters**

601

602 The whole computational domain includes the Tanjiashan Lake in the most upstream area and
603 1.85 km downstream of the Old Town of Beichuan, with a total length of 8.6 km. The plan
604 view and topographic contours of the computational area are shown in Fig. 19 (a) and (b).
605 According to the field survey, the river channel upstream of the Beichuan Hotel has a bed
606 roughness of $n = 0.042$ and the downstream area from this location has $n = 0.04$. The
607 numerical simulations aim to reproduce the flooding and sediment process for the next 7 days
608 after the dam break flow disaster. For the boundary conditions, the upstream inflow
609 hydrograph and downstream rating curve are shown in Fig. 20 (a) and (b), respectively.

610

611



612

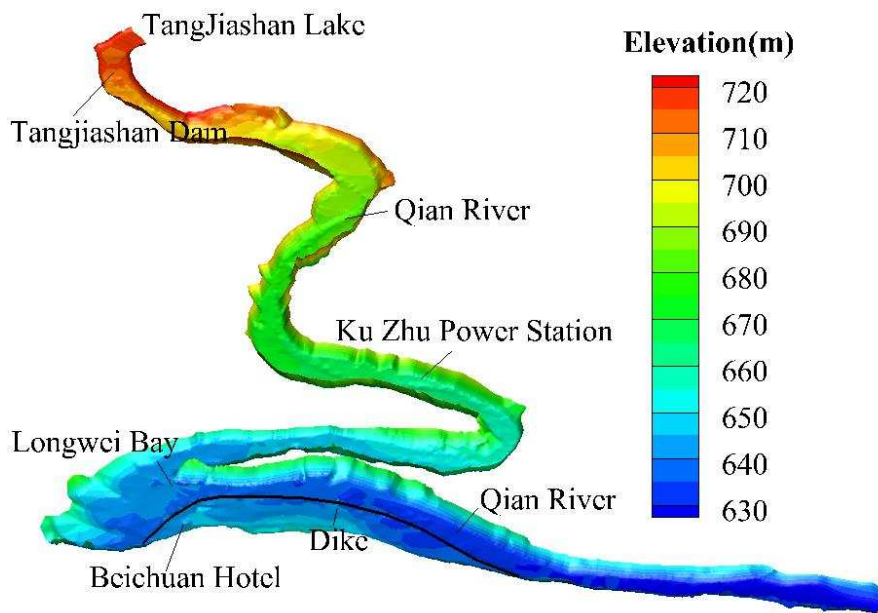
613

614

615

616

(a)



617

618

619

620

(b)

621 **Fig. 19 (a) Plan view; (b) Topographic contours of computational domain, including key**
622 **control locations**

623

624

625

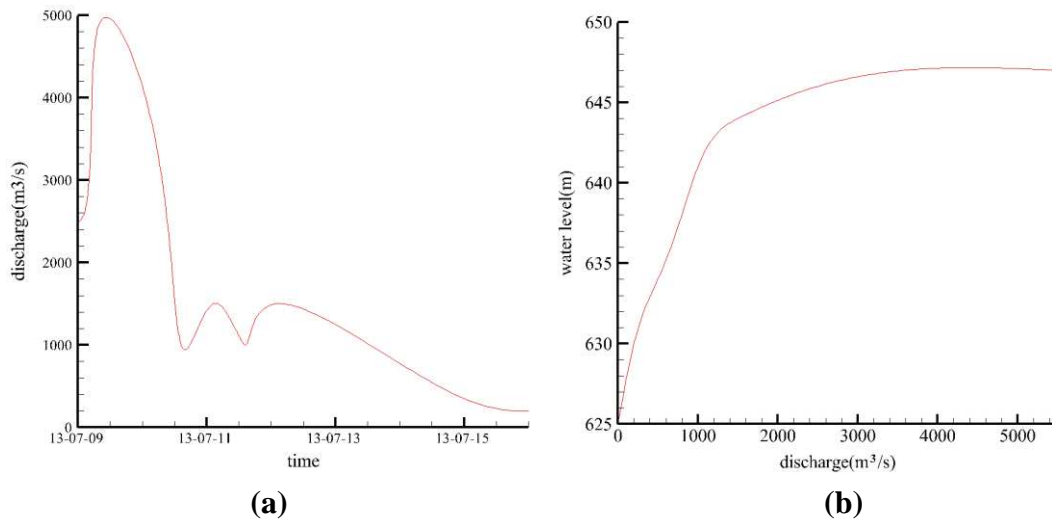


Fig. 20 (a) Upstream hydrograph; (b) Downstream rating curve for model input

627
628
629
630
631
632
633
634
635
636
637
638
639
640
641
642
643
644
645

At the beginning of the computation, the river channel is treated as being dry. As described by Chen et al. (2011), in order to obtain a good-shaped wet-dry boundary line, a minimum threshold water depth h_{\min} is used. A node is regarded as being dry when its water depth is less than h_{\min} , otherwise it is marked as being wet. A grid including any dry node is treated as a dry grid unless it contains all of the wet nodes, in which case it is regarded as being wet. The upstream sediment input is assumed to be from the breached dam materials rather than from the Tanjishan Lake area. The bed materials of the channel are composed of three layers and the sediment size gradations for each layer are shown in Table 2 as below.

Table 2. Sediment layer thickness and grain size gradation of each layer

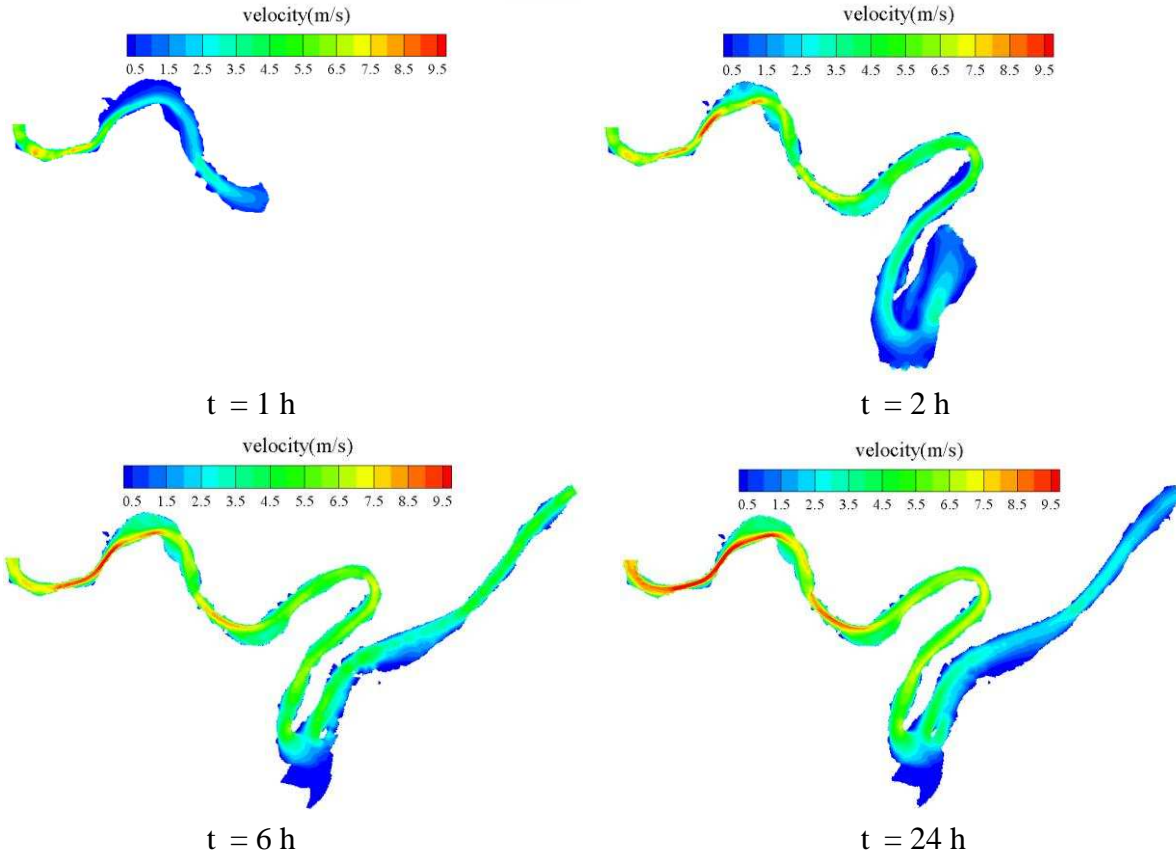
Sediment layer thickness (m)	Gradation of sediment grain size in percentage (%)					
	200~60	60~20	20~5	5~2	0.5~0.25	<0.25
Sediment size (mm)	200~60	60~20	20~5	5~2	0.5~0.25	<0.25
2 (upper layer)	37.2	27.8	16.3	6.6	6.7	3.4
2 (middle layer)	24.8	24.5	18.3	12.1	15.5	4.8
5 (lower layer)	48.2	14.6	8.2	10.2	14.4	4.4

646
647
648
649

650 **5.2.3 Modeling results and discussions**

651

652 Fig. 21 shows the computed velocity fields after the dam break flood at time $t = 1$ h, 2 h, 6 h,
653 24 h, 3 d and 7 d, respectively. It shows that the flooding water propagates about 2.9 km
654 downstream of the dam at $t = 1$ h. The flow velocities decrease from the dam site, which are
655 around 5.0 m/s, to about 1.0 m/s towards the downstream region due to the widening of the
656 channel and the flow energy dissipation from bed friction. At $t = 2$ h, the flood flow reaches
657 the downstream of Longwei Bay with a smaller front velocity of 1.2 m/s as a result of the
658 spacious flow path. It has been observed in the model simulation that the flow arrives at the
659 outlet boundary of the model at time $t = 2.7$ h. Due to the continuous supply of flooding
660 water from the dam reservoir, the general velocity amplitude increases at $t = 6$ h, which is
661 demonstrated by the fact that the main flow velocity upstream of the Longwei Bay exceeds 5
662 m/s ~ 10 m/s, while the corresponding downstream velocity is also as high as 3 m/s ~ 5 m/s.
663 After $t = 24$ h of the dam break, due to the reduction of the upstream flood input, the general
664 flow velocities tend to decrease. However, due to the erosion of the upstream main channel,
665 the converged water still maintains sufficient momentum. Between $t = 3$ d and 7 d, the flow
666 velocities start to demonstrate a decreasing trend, due to the continuous reduction in the
667 upstream water supply. Finally, all of the flooding water returns to the main channel and there
668 exists a clear difference in the flow patterns at upstream and downstream of the Longwei Bay.
669



670

671

672

673

674

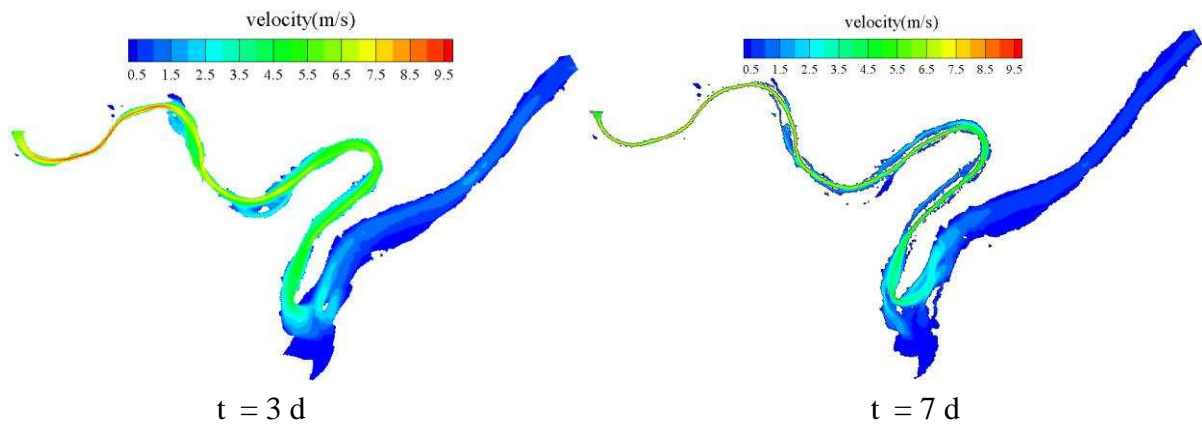
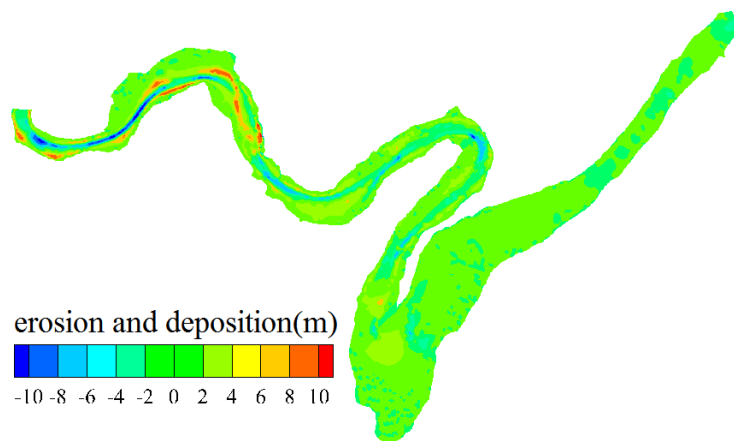
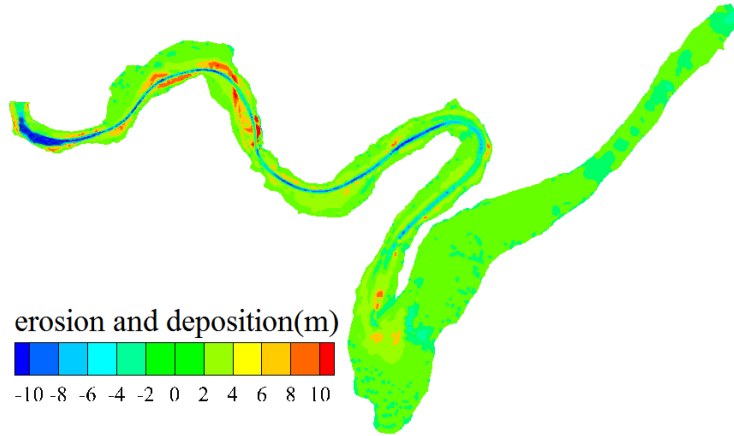


Fig. 21 Computed velocity fields of flood flow at different times

The sediment erosion and deposition of the river bed are shown in Fig. 22 for the next three days after the dam break flood. It is shown that by one day later, most of the alluvial processes happen near the dam area. This is demonstrated by the fact that severe erosions are found immediately downstream of the Tongjiashan Dam and further downstream channels show the features of erosion in the main channel and deposition on the side bank. Then three days later, the erosion of the main channel has progressed to somewhere upstream of the Longwei Bay. Finally seven days after the dam break, a quasi-equilibrium state of the alluvial evolution has achieved, demonstrated by the clear erosion of the main channel which deposited the sediment materials onto the side bank. The deposition thickness near the Longwei Bay reaches as high as 5 ~ 10 m.

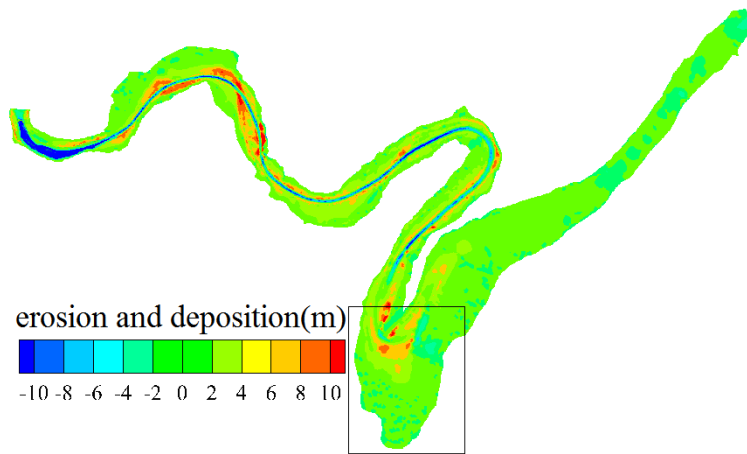


(a) Day one



695
696
697

(b) Day three



698
699
700
701

(c) Day seven

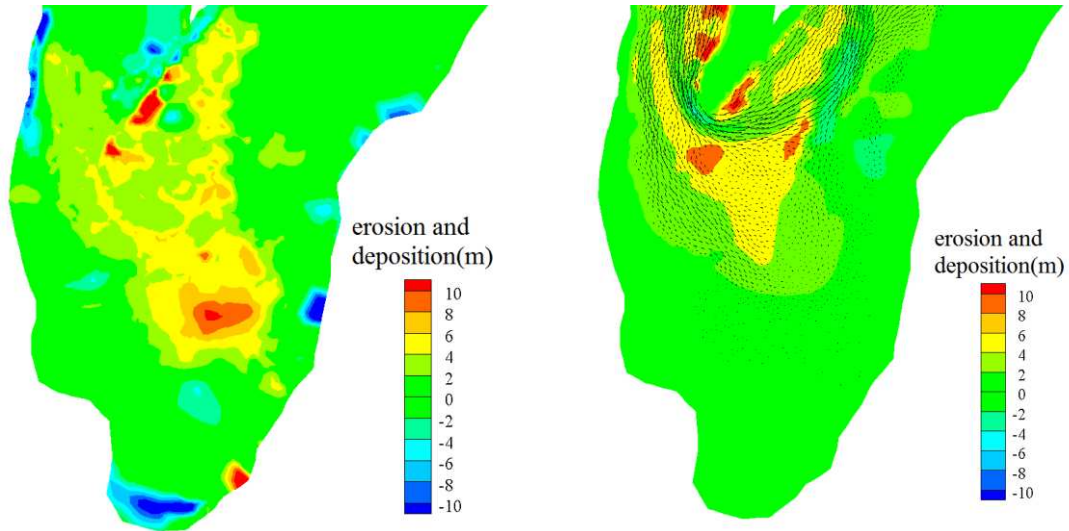
Fig. 22 Alluvial process of dam break flood in downstream areas

702
703
704

705 To validate the model simulations, the alluvial pattern of the bed on 7th day is compared with
706 the field observations in Fig. 23 and the computed flow inundation depth near the Beichuan
707 Hotel is shown in Fig. 24 (for the enlarged area as indicated by the square in Fig. 22). The
708 comparisons in Fig. 23 show a similar deposition pattern near the Longwei Bay between the
709 numerical results and field observations. The differences lie in that the measured thickness of
710 the deposit is higher than that from the numerical simulations by about 2.0 m near the front of
711 the alluvial fan. Besides, the discrepancy also appears in the deposition area of the main
712 channel and side bank. This could be due to that in the numerical model, the sediment
713 movement is controlled by the flow velocity field and the smaller velocity calculated on the
714 side bank cannot transport much sediment material. However, in the practice some hyper-
715 concentrated flows in the form of slurry have been found on the surface of the deposits which
716 continued to move downstream to reshape the alluvial process. Furthermore, the

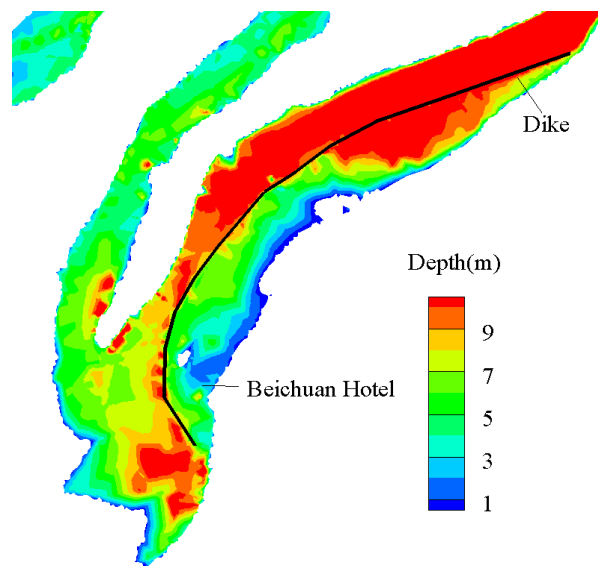
717 simplifications of initial and boundary conditions in the numerical model could also cause
 718 uncertainty in the result predictions. In addition, the inundation depths computed in Fig. 24
 719 indicate that most of the areas near the Beichuan Hotel and Dike have been deposited by the
 720 sediments up to more than 8.0 m. This is also quite consistent with the field observations and
 721 the media report.

722
 723



724
 725
 726
 727
 728
 729
 730

Fig. 23 Alluvial pattern of bed 7 days after the dam-break flood (left: field observation; right: numerical result)



731
 732
 733
 734

Fig. 24 Computed flow inundation depths near Beichuan Hotel and Dike area

735 **6. Conclusions**

736

737 The paper combined the FEM characteristic splitting method and FVM Godunov scheme and
738 developed a water-sediment mixture flow model for the field river studies in Southwest
739 China. The FEM numerical algorithm is robust for the treatment of advection term and
740 flexible in fitting the complicated physical boundary, while the FVM solution scheme has
741 satisfactory conservation property and numerical accuracy. Through a series of benchmark
742 unsteady flow tests and two field case applications, the hybrid FEM-FVM model has been
743 found to have good stability and accuracy when the numerical results were compared with the
744 experimental data. The study demonstrates that the present numerical model could provide a
745 simple and useful prediction tool for the water-sediment mixture flow problems in
746 engineering field as an economic substitute for the physical experiment and field observation.

747

748 In order to more accurately forecast the practical sediment transport and alluvial deformation,
749 more sound sediment erosion and deposition mechanisms should be explored in the future
750 work. As fundamental sediment properties could behave significantly different from one
751 region to another (Wang and Zhang, 2012), further investigations on the sediment initiation,
752 sediment-laden capacity, sediment settling velocity, etc. should be of more priority than the
753 development of higher-order numerical schemes. This is especially true shall the model be
754 applied to the practical field cases in different regional areas.

755

756 Finally, we would like to mention that the main objective of the present research is to use the
757 numerical model to evaluate the dam break flood in the downstream areas. However, in many
758 engineering situations, the upstream flow structures and sediment erosion and sedimentation
759 properties, such as the dam-failure hydrograph and morphological changes at the dam site,
760 are of particular interest in the engineering community as documented by Wang et al. (2008)
761 and Liu et al. (2012). Also, these could provide a more robust test on the capacity of the
762 numerical models.

763

764

765 **Acknowledgements**

766

767

768 This research work is supported by the Start-up Grant for the Young Teachers of Sichuan
769 University (No. 2014SCU11056), National Science and Technology Support Plan (No.
770 2012BAB0513B0) and Open Fund of the State Key Laboratory of Hydraulics and Mountain
771 River Engineering, Sichuan University (No. SKHL1409). Finally, we kindly acknowledge the
772 constructive discussions with Dr Jaan Hui Pu at Bradford University, UK during the
773 manuscript preparations.

774

775 **References**

776

777 Brufau, P., Garcia-Navarro, P. and Vazquez-Cendon, M. E. (2004), Zero mass error using
778 unsteady wetting-drying conditions in shallow flows over dry irregular topography,
779 *International Journal for Numerical Methods in Fluids*, 45(10), 1047-1082.

780

781 Cantelli, A., Paola, C. and Parker, G. (2004), Experiments on upstream-migrating erosional
782 narrowing and widening of an incisional channel caused by dam removal, *Water Resources*
783 *Research*, 40, W03304, doi:10.1029/2003WR002940.

784

785 Cao, Z. X., Yue, Z. Y. and Pender, G. (2011), Landslide dam failure and flood hydraulics. Part
786 II: coupled mathematical modelling, *Natural Hazards*, 59, 1021–1045.

787

788 Casulli, V. and Zanolli, P. (2002), Semi-implicit numerical modeling of nonhydrostatic free
789 surface flows for environmental problems, *Mathematical and Computer Modeling*, 36, 1131-
790 1149.

791

792 Chen, R. D. (2011), *Mathematical Modeling of Mountainous Rivers*, PhD Dissertation,
793 Sichuan University, Chengdu, China (in Chinese).

794

795 Chen, R. D., Liu, X. N., Cao, S. Y. and Guo, Z. X. (2011), Numerical simulation of deposit in
796 confluence zone of debris flow and mainstream, *Science China Technological Sciences*,
797 54(10), 2618-2628.

798

799 Demirbilek, Z. and Nwogu, O. G. (2007), Boussinesq modeling of wave propagation and
800 runup over fringing coral reefs, Model Evaluation Report, Technical Rep. No. ERDC/CHL
801 TR-07-12, U.S. Army Corps of Engineers, Vicksburg, MS.

802

803 Du, C. J. (2000), An element-free Galerkin method for simulation of stationary two-
804 dimensional shallow water flows in rivers, *Computer Methods in Applied Mechanics and*
805 *Engineering*, 182, 89-107.

806

807 Guillou, S. and Nguyen, K. D. (1999), An improved technique for solving two-dimensional
808 shallow water problems, *International Journal for Numerical Methods in Fluids*, 29, 465-483.

809

810 Liu, F., Fu, X. D., Wang, G. Q. and Duan, J. (2012), Physically based simulation of dam
811 breach development for Tangjiashan Quake Dam, *China Environ Earth Sci*, 65, 1081–1094.

812

813 Liu, H. F., Li, M. and Shu, A. P. (2012), Large eddy simulation of turbulent shallow water
814 flows using multi-relaxation-time lattice Boltzmann model, *International Journal for*

815 Numerical Methods in Fluids, 70, 1573-1589.
816
817 Liu, X. N. (2004), Gravel Bed Load Movement and Modeling, PhD Dissertation, Sichuan
818 University, Chengdu, China (in Chinese).
819
820 Liu, X. N., Chen, Y. X. and Li, H. (1991), Study of near bed sediment movement by using
821 high-speed photographing, Sediment Research, 1, 57-60 (in Chinese).
822
823 Pu, J. H., Cheng, N. S., Tan, S. K. and Shao, S. D. (2012), Source term treatment of SWEs
824 using surface gradient upwind method, Journal of Hydraulic Research, 50, 145-153.
825
826 Qian, N. and Wan, Z. H. (1983), Sediment Transport Mechanics, Scientific Publishing (in
827 Chinese).
828
829 Soares-Fraza, S., Canelas, R., Cao, Z. X., Cea, L., Chaudhry, H. M., et al. (2012), Dam-
830 break flows over mobile beds: experiments and benchmark tests for numerical models,
831 Journal of Hydraulic Research, 50(4), 364-375.
832
833 USACE (2003), HEC Geospatial Hydrological Modeling Extension User's Manual, US Army
834 Corps of Engineers, Research Center in Water Resources, University of Texas.
835
836 Wang, G. Q. (1999), Review of sediment issues in China, Advances in Water Sciences, 3,
837 337-344 (in Chinese).
838
839 Wang, G. Q., Liu, F., Fu, X. D. and Li, T. J. (2008), Simulation of dam breach development
840 for emergency treatment of the Tangjiashan Quake Lake in China, Sci China Ser E - Tech Sci,
841 51(Supp. II), 82-94.
842
843 Wang, Z. Y. and Song, Z. Q. (1995), Review of sediment study in Europe and America,
844 Proceedings of Second National Symposium on Fundamental Sediment Theory, Beijing
845 Construction and Material Industry Publisher, 3-15 (in Chinese).
846
847 Wang, Z. Y. and Zhang, K. (2012), Principle of equivalency of bed structures and bed load
848 motion, International Journal of Sediment Research, 27, 288-305.
849
850 Zhang, R. J. (1961), Alluvial Dynamics, China Industry Publishing (in Chinese).
851
852 Zhang, R. J. (1998), Alluvial and Sediment Dynamics, China Hydraulic and Hydroelectric
853 Publishing (in Chinese).
854

855 Zienkiewicz, O. C. and Codina, R. (1995), A general algorithm for compressible and
856 incompressible – flow. 1. The split, characteristic-based scheme, International Journal for
857 Numerical Methods in Fluids, 20, 869-885.